Accurate *ab initio* modeling of solid solution strengthening in high entropy alloys

Franco Moitzi,[1] Lorenz Romaner,[2] Andrei V. Ruban,[1,3] and Oleg E. Peil[1]

[1]*Materials Center Leoben Forschung GmbH, Roseggerstraße 12, A-8700 Leoben, Austria*

[2]*Chair of Physical Metallurgy and Metallic Materials, Department of Materials Science, University of Leoben, Roseggerstraße 12, A-8700 Leoben, Austria*

[3]*Department of Materials Science and Engineering, Royal Institute of Technology, 10044 Stockholm, Sweden*

(Received 29 July 2022; accepted 29 September 2022; published 24 October 2022)

High entropy alloys (HEA) represent a class of materials with promising properties, such as high strength and ductility, radiation damage tolerance, etc. At the same time, a combinatorially large variety of compositions and a complex structure render them quite hard to study using conventional methods. In this work, we present a computationally efficient methodology based on *ab initio* calculations within the coherent potential approximation. To make the methodology predictive, we apply an exchange-correlation correction to the equation of state and take into account thermal effects on the magnetic state and the equilibrium volume. The approach shows good agreement with available experimental data on bulk properties of solid solutions. As a particular case, the workflow is applied to a series of iron-group HEA to investigate their solid solution strengthening within a parameter-free model based on the effective medium representation of an alloy. The results reveal intricate interactions between alloy components, which we analyze by means of a simple model of local bonding. Thanks to its computational efficiency, the methodology can be used as a basis for an adaptive learning workflow for optimal design of HEA.

DOI: 10.1103/PhysRevMaterials.6.103602

I. INTRODUCTION

Concentrated solid solutions with multiple components, also known as high entropy alloys (HEA), have attracted a lot of attention because of their exceptional combination of yield strength and ductility [1–5]. Although the highest strength is usually achieved in multiphase alloys, HEAs are characterized by a high yield strength even in the form of single-phase solid solutions [3]. Especially interesting in this respect are face-centered-cubic (fcc) HEAs, where a high ductility can coexist with high strength beyond the usual tradeoff [6]. The high strength in these systems is mainly associated with the interaction of dislocations with solutes, which impedes the motion of dislocations, resulting in the solid solution strengthening (SSS).

Direct modeling of dislocation motion in multicomponent alloys is currently possible only within semiempirical approaches such as classical molecular dynamics [7–9], which provide a qualitative picture. At the same time, comparable *ab initio* simulations of dislocations are not feasible, and one has to combine them with phenomenological models, reducing the complex problem of a dislocation interacting with alloy components to a set of parameters (e.g., effective atomic volumes, elastic moduli, the stacking fault energy, etc.) that can be obtained by first-principles calculations.

Recently, Varvenne and Curtin (VC) have proposed a generalized model that does not rely on any assumptions about the concentration of components and it is specifically designed to treat HEA systems [10,11]. Similar to earlier dilute-limit models [12–14], the central mechanism of the VC model is the occurrence of energy barriers for dislocation motion due to local effective volume fluctuations caused by alloy components, which increases the stress for the onset of dislocation glide and hence the yield strength [10]. The system is treated as an effective alloy matrix with solutes interacting with the matrix by means of stress fields caused by the atomic-size mismatch between a solute and the effective matrix element. Thanks to the low Peierls stress in face-centered-cubic (fcc) metals, the yield stress is then expressed solely in terms of the average misfit volume of components and linear elastic properties of the alloy. An important feature of the VC model is that it suggests that the strengthening effect does not directly depend on the number of components and is not necessarily maximized by the equimolar composition often used in experimental work [15]. Instead, the largest yield stress is achieved by maximizing the average mean-square misfit volume, while minimizing a potential negative impact on the elastic properties. This is consistent with experimental evidence that nonequimolar compositions can show significantly improved mechanical properties as compared to alloys with equimolar ratios of principal elements [16,17].

The VC model has been successfully applied to a number of systems [18–23]. However, in most of the cases the model parameters have been determined or estimated from experimental data, which limits the applicability and predictive power of the model. On the other hand, these parameters could be calculated *ab initio* using the density functional theory (DFT), but the accuracy of the calculation is strongly affected by the general error that most widely used (semi)local exchange-correlation (XC) functionals produce for the

equilibrium volume of an alloy or an element in its ground state. This leads to an overall discrepancy both in the average molar volume of the alloy and in the misfit volumes of constituent elements [22]. The situation becomes even more involved in the case of HEA based on the iron group of 3*d* metals, where finite-temperature magnetism plays an important role for relevant temperatures of interest, usually ranging from room temperature to 1000 K and above.

In this work, we address the above-mentioned limitations of DFT-based modeling by proposing a computationally inexpensive methodology based on the coherent potential approximation (CPA) [24,25], which offers a very consistent way of describing properties of the effective alloy medium underlying the VC model.

Within this approach, the equilibrium volumes are adjusted using element-specific corrections, which, in turn, improve other equilibrium properties. Our methodology also takes into account finite-temperature effects mediated by magnetic and phonon degrees of freedom, which are especially important for describing the temperature dependence of SSS above room temperature. We create a fully automatized workflow for calculating all necessary quantities for estimating SSS and demonstrate it on several well-studied 3*d* transition metal HEAs, which are well known for their complex magnetic behavior.

II. METHODS

A. Exchange-correlation pressure correction

The use of local [e.g., local density approximation (LDA)] or semilocal [e.g., generalized gradient approximation (GGA)] exchange-correlation functionals within DFT is known to lead to systematic errors in equilibrium properties of solids. Multiple attempts to improve XC functionals have been made [26–30] but due to general limitations of semilocal density functionals [31] these implementations often improve the accuracy for only certain classes of solids, while failing to do so for others.

One can distinguish two types of errors: (1) the error in the equilibrium volume (or lattice constant), and (2) the error in the value of a target quantity at the exact experimental volume. The motivation for this distinction comes from the empirical observation that many linear-response properties can be reproduced reasonably well even by the local density approximation without gradient corrections, provided that a calculation is performed at the experimental equilibrium volume [32]. Whereas type-2 errors are intrinsic to an XC functional and cannot be remedied without reconsidering the XC functional itself, type-1 errors can be estimated and eliminated since the equilibrium volume of practically all pure elemental materials is known experimentally, and we only need to find a way how to use this information to correct for the volume error of a compound. A naive interpolation of volumes or lattice constants (Vegard's law) from experimental values for pure elements will definitely give poor results because the interaction between different elements in a compound is completely ignored in this case. Another approach is to apply linear interpolation only to the deviations between DFT and experimental results [33]. This way one can get much better results for solid solutions of similar elements but this methodology is not well justified in cases when the ground-state structure of components is different from the structure of an alloy. For example, it is not clear how one could correct for the error in determining the equilibrium volume of a hypothetical zero-temperature fcc structure of Fe (which can serve as a reference for Fe-based fcc alloys) from the error in the actual ground-state body-centered-cubic (bcc) structure.

A different approach was put forward by van de Walle and Ceder [34] who argued that there is an intrinsic source of errors in the traditional XC functionals (LDA, GGA, meta-GGA) related to their semilocal nature. Based on their systematic study of the error in the equilibrium volume of multiple ordered compounds they concluded that this error can be largely attributed to a nonlocal contribution responsible for a significant modification of the exchange-correlation hole of interstitial (valence) electrons in the region predominantly occupied by highly localized core electrons.

Under certain rather general assumptions about the form of this nonlocal contribution, they concluded that its effect on the total energy can, to a first approximation, be taken into account by adding to the local density functional another term that is linear in volume. This results in an additional *pressure* correction associated with each atom in a compound.

Importantly, this correction turns out to be also linear in concentration, implying that most of the error in the calculation of the equation of state can be eliminated by introducing an XC pressure correction (XPC), P_{XC}, given by a sum of individual element-specific contributions $P_{\mathrm{XC}} = \sum_i m_i P_{\mathrm{XC}}^{(i)}$ for elements i of a unit cell, with m_i denoting the element multiplicity. The linear dependence of P_{XC} on concentrations makes the above ansatz readily applicable to disordered alloys, where the XC pressure correction will be given by $\langle P_{\mathrm{XC}} \rangle = \sum_i c_i P_{\mathrm{XC},i}^{(i)}$ with c_i being the atomic fractions of alloy components i. Moreover, the simple form of the correction makes it compatible with the CPA for disordered systems [24,25], suggesting a simple and efficient approach for accurate evaluation of the equilibrium volumes and other properties of solid solutions.

Given the known experimental zero-temperature equilibrium volume $V_{\mathrm{eq}}^{(i)}$ (corrected for zero-point vibrations), of element i, the parameter $P_{\mathrm{XC}}^{(i)}$ correcting a given XC functional, say LDA, can be determined from

$$P_{\mathrm{XC}}^{(i)} = -P_{\mathrm{LDA}}^{(i)}\left(V_{\mathrm{eq}}^{(i)}\right), \tag{1}$$

where $P_{\mathrm{LDA}}^{(i)}(V)$ is the LDA (pressure) equation of state for element i. This ensures that the corrected pressure $P_{\mathrm{LDA}}^{(i)}(V) + P_{\mathrm{XC}}^{(i)}$ equals zero at the exact experimental volume.

Once the average parameter $\langle P_{\mathrm{XC}} \rangle$ is known, the corrected equation of state reads as

$$\overline{E}(V) = \Delta E_{\mathrm{XC}} + E_{\mathrm{LDA}}(V) - \langle P_{\mathrm{XC}} \rangle V, \tag{2}$$

where $E_{\mathrm{LDA}}(V)$ is the equation of state within the LDA functional and ΔE_{XC} is a constant correction term. This term, ΔE_{XC}, can be estimated in the same fashion as the pressure from the difference between the theoretical and experimental cohesive energies. However, it cancels out for most of the properties that preserve species balance and we, therefore, do not consider it in this work. The correction for other semilocal

functionals, such as Perdew-Burke-Ernzenhof (PBE) [35] or Perdew-Wang (PW91) [36], is formulated in a similar way.

In this work, we use the exact muffin-tin orbital (EMTO) [37] code (Lyngby version [38]) implementing a Green's function based DFT methodology combined with CPA to perform total-energy calculations. Screened Coulomb interactions in the CPA are obtained by the use of the locally self-consistent Green's function technique [39] implemented also within the EMTO method [40]. The total energy is obtained within the full charge density formalism [41], making the results comparable to those from full potential codes. The paramagnetic state of metallic alloys is described using the disordered local moment (DLM) approach [42].

B. Finite-temperature effects

Most of the experimental results for alloys are obtained at room temperature. Moreover, for many technological alloys it is vital to understand their behavior at even higher temperatures. We, therefore, need to extend calculations of the equation of state to finite temperatures. For the ambient pressure we replace the total energy with the Helmholtz free energy

$$F(V,T) = F_{\mathrm{el}}(V,T) + F_{\mathrm{ph}}(V,T), \tag{3}$$

where we consider two main contributions: electronic, $F_{\mathrm{el}}(V,T)$, containing the XC pressure correction as well as eventual high-temperature magnetic fluctuations, and phonon, $F_{\mathrm{ph}}(V,T)$. Such a decomposition is possible because phonon degrees of freedom evolve on a much longer timescale than the electronic ones.

The electronic part of the free energy can, in turn, be split into the one-electron part $F_{\mathrm{one}}(V,T)$ and the magnetic part $F_{\mathrm{mag}}(V,T)$. The one-electron entropy is calculated using the usual Sommerfeld formula with energy contour integration weighted by the Fermi function. Unlike the one-electron part, the magnetic contribution to the free energy $F_{\mathrm{mag}}(V,T)$ is more difficult to tackle in a consistent manner. Although DLM is supposed to describe the paramagnetic state at high temperatures, in its original form it works only for elements (Fe and Mn) which preserve the localized character of spin magnetic moments in the DLM state. To get the correct magnetic behavior for elements with primarily itinerant character of magnetism (Cr, Ni, Co) one has to take into account temperature-induced longitudinal spin fluctuations (LSF). In this work, we use a semiclassical model presented earlier in Refs. [38,43]. Within this model, we perform DLM calculations and take into account LSF by adding an entropic contribution $-TS_{\mathrm{mag}}[M]$ to the electronic free energy and to the self-consistent potential. Here, M is the magnetic moment of a specific component obtained self-consistently within the DFT cycle. For elements with primarily itinerant magnetic character, the entropy has a form $S_{\mathrm{mag}}[M] = a \log M$, where coefficient a is element specific and furthermore depends on the magnetic behavior of an element in a particular alloy system. The coefficient can be chosen based on a series of fixed-spin-moment calculations for the element in a given alloy [38]. For elements with more localized behavior, i.e., Fe (at large volumes) and Mn, the entropy term is taken to be equal to $S_{\mathrm{mag}}[M] = \log(1+M)$. We note that this model of LSF has been producing very consistent results for alloys based on iron-group metals, including Fe-based fcc solid solutions, which is generally a rather difficult case for modeling [33,44–46].

TABLE I. Alloys used for testing the pressure correction on equilibrium volume and bulk modulus.

Composition	Magnetic state	T (K)	Structure	Ref.
Ni	Paramagnetic	700	fcc	[49,50]
NiCo	Paramagnetic	300	fcc	[51]
NiCoCr	Paramagnetic	300	fcc	[51]
NiCoCrMnFe	Paramagnetic	300	fcc	[51,52]
NiCoFe	Paramagnetic	300	fcc	[51]
NiCoCrFe	Paramagnetic	300	fcc	[51]
Fe0.2Cr0.8	Paramagnetic	300	bcc	[53,54]
Fe0.88Co0.8	Ferromagnetic	300	bcc	[53]
W0.3Cr0.7	Nonmagnetic	300	bcc	[55]
W0.8Cr0.2	Nonmagnetic	300	bcc	[55]
Fe0.94Re0.06	Paramagnetic	300	bcc	[53]

The phonon free energy is calculated within the Debye-Grüneisen model [47,48], with the parameters (the bulk modulus, the Grüneisen constant) derived from the equation of state calculated at the respective temperature. This way, basic coupling between magnetic and phonon degrees of freedom related to the volume dependence of the magnetic moment (the invar/anti-invar effect) is taken into account.

The described methodology was benchmarked by applying it to a series of alloys for which reliable experimental data on the equilibrium volume and elastic properties are available (Table I). For reference calculations of magnetic 3*d* metals their respective ground-state magnetic structures were considered. The spin-density wave magnetic state of Cr was approximated by a collinear antiferromagnetic state of [001] type. The magnetic state of α-Mn has been approximated by a collinear antiferromagnetic state structure [56].

In the calculations with XC pressure correction we choose LDA as the reference functional. This choice is motivated, on one hand, by better magnetic moments that this functional tends to produce at the experimental volume. On the other hand, the relatively large error in the equilibrium volume is anyway corrected by the pressure correction. In contrast to LDA, the most commonly used gradient approximation, PBE, is known to overestimate magnetic effects [32,57] and it is, hence, less preferable for systems where magnetism is crucial. The results of the benchmark calculations with LDA-XPC compared to a fully *ab initio* PBE and to experimental data [50–55,58–60] are displayed in Fig. 1. Pure LDA results were omitted from the figure due to their largely underestimated equilibrium volumes compared to LDA-XPC and PBE. As one can see, equilibrium volumes obtained with LDA-XPC calculations are in better agreement with experiment for most of the cases except for three systems where PBE performs slightly better but both methods give a rather small error in these cases. At the same time, when it comes to the bulk modulus, LDA-XPC always performs significantly better than PBE, reducing the relative error from more than 16% to less than 10%.

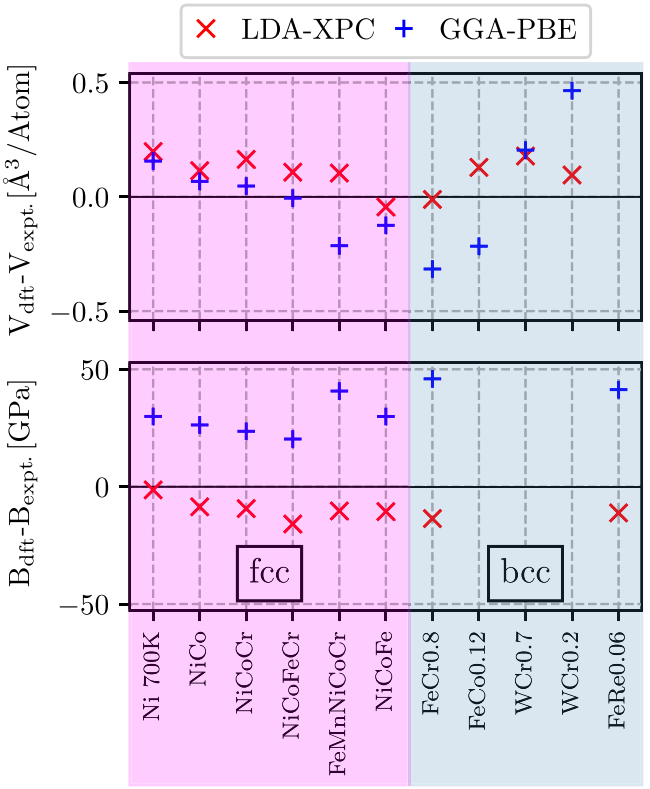

FIG. 1. Comparison of the experimental and calculated atomic volume and bulk modulus for disordered paramagnetic and nonmagnetic alloys. (× red): LDA with XC pressure correction (LDA-XPC). (+ blue): PBE. Phonon contributions to the thermal expansion are included in all cases. Magnetic entropy is considered for the paramagnetic alloys.

C. Solid solution strengthening

The VC model predicts the critical resolved shear stress (CRSS) at any temperature and strain rate for any given alloy composition, with CRSS defined as a stress required to initiate slip in a perfect single crystal. It can be considered as a material-specific and temperature-dependent constant, independent of the microstructure of a sample and the specific measurement method. In HEAs considered in this work, the CRSS is mostly determined by SSS since the Peierls stress can be disregarded in fcc random alloys [10,61].

Within the VC model, the temperature-dependent yield stress is characterized by two thermal activation models specific to certain temperature ranges. In the low-temperature range, $\Delta\tau(T)$ is given by

$$\Delta\tau(T) = \tau_{y0}\left[1 - \left(\frac{kT}{E_b}\ln\frac{\dot{\varepsilon}_0}{\dot{\varepsilon}}\right)^{\frac{2}{3}}\right], \tag{4}$$

whereas for higher temperatures,

$$\Delta\tau(T) = \tau_{y0}\exp\left(-\frac{1}{0.51}\frac{kT}{E_b}\ln\frac{\dot{\varepsilon}_0}{\dot{\varepsilon}}\right). \tag{5}$$

Both models give essentially equal results for moderate temperature range (100–400 K). We employ, therefore, the high-temperature model only for calculations above 400 K, where some notable difference can be seen. In the above equations, τ_{y0} and E_b are, respectively, the zero-temperature yield stress and the activation barrier, given by the following expressions:

$$\tau_{y0} = A_\tau\left(\frac{\Gamma}{b^2}\right)^{-\frac{1}{3}}\left(\mu^V\frac{1+\nu^V}{1-\nu^V}\right)^{\frac{4}{3}}\delta^{\frac{4}{3}}, \tag{6}$$

$$\Delta E_b = A_E\left(\frac{\Gamma}{b^2}\right)^{\frac{1}{3}}b^3\left(\mu^V\frac{1+\nu^V}{1-\nu^V}\right)^{\frac{2}{3}}\delta^{\frac{2}{3}}, \tag{7}$$

with b, $\Gamma = \alpha\mu_{\langle 110\rangle/\{111\}}b^2$ being the Burgers vector and the dislocation line tension ($\alpha = 0.125$ is the edge dislocation line tension parameter for fcc metals); $\mu_{\langle 110\rangle/\{111\}}$ is the shear modulus for fcc slip on the $\{111\}$ plane in the $\langle 110\rangle$ direction; μ^V and ν^V are the Voigt average of shear modulus and Poisson's ratio, respectively; δ is the misfit parameter describing the collective effect of the individual solute misfit volumes.

The reference strain rate $\dot{\varepsilon}_0$ is set to 10^4 s^{-1} as in previous works [22]. The actual strain rate $\dot{\varepsilon}$ is always set to be the same as in the respective experiment. Prefactors $A_\tau = 0.048\,65\,[1-(A-1)/40]$ and $A_E = 2.5785\,[1-(A-1)/80]$ are associated with a typical fcc dislocation core structure consisting of two well-separated partial dislocations plus a small correction for elastic anisotropy related to the Zener anisotropy $A = 2C_{44}/(C_{11}-C_{12})$.

Note that apart from the explicit temperature dependence, all material parameters entering the expressions can be temperature dependent by themselves. For instance, elastic moduli generally decrease with temperature, while the lattice constant (hence the volume and Burger's vector b) increase. This has often been neglected in earlier works but, as we will show in the next section, these additional temperature dependencies lead to an effective thermal behavior deviating from the naive Arrhenius law.

The central quantity of the VC model that introduces the chemical dependence of the dislocation-solute interaction is the misfit parameter $\delta = \sqrt{\sum_i c_i(\Delta V_i)^2}/(3V_{\text{alloy}})$, where ΔV_i are element-specific misfit volumes

$$\Delta V_i = V_i - V_{\text{alloy}}, \tag{8}$$

with V_{alloy} being the specific atomic volume of the alloy and V_i the *apparent* (effective) volume of alloy component i. The misfit volumes themselves are expressed in terms of concentration derivatives of the alloy volume,

$$\Delta V_i = \frac{\partial V_{\text{alloy}}}{\partial c_i} - \sum_j c_j\frac{\partial V_{\text{alloy}}}{\partial c_j}, \tag{9}$$

and the derivatives can be calculated by numerical differentiation. To get these derivatives in practice, we perform a series of CPA calculations for systems with small deviations from the composition of the original alloy. The obtained volume points are then fitted to a linear function of concentration. Based on convergence tests (see Appendix A), we found that four volume points per alloy component, with the concentration of the respective element varied by $-\delta$, $-\delta/2$, $\delta/2$, δ ($\delta = 0.012$) with respect to the original alloy, is sufficient to get reliable derivatives $\frac{\partial V_{\text{alloy}}}{\partial c}$. For an N-element alloy $4\times N+1$ calculations are performed including the original alloy composition. The linear elastic constants are obtained from volume-conserving monoclinic and orthorhombic

distortions following the computational details described in Refs. [62,63].

Local lattice relaxations induced by the atomic-size mismatch of the alloy components have found to be essential for the stability and properties of HEA. As a single-site theory, CPA does not take into account local lattice distortions. However, previous supercell calculations of special quasirandom structures (SQS) [64,65] showed that the equilibrium parameters involved in the VC model are not significantly affected by local lattice distortions. Upon including relaxation explicitly, the change in the lattice parameter for iron-group fcc HEA was found to be around 0.1%–0.2%. Also, the effect on the elastic constants was reported as insignificant in the case of similar sized constituents.

III. RESULTS

We applied the methodology described in the previous sections to calculate and analyze solid solution strengthening of three alloys: NiCoCr, FeNiCoCr, and FeMnNiCoCr. All of them are well studied both experimentally and theoretically, which enables us to carry out an extensive benchmarking.

A. NiCoCr

The solid solution alloy NiCoCr is a rare example where a direct experimental measurement of misfit volumes was undertaken [23]. At the same time, DFT simulations accompanying experiment in Ref. [23] showed significant deviations both in misfit and apparent volumes. This system, thus, represents an ideal case for testing our proposed methodology. First, we perform calculations at room temperature where most of the SSS measurements are done. Since the equimolar NiCoCr alloy is already paramagnetic above 4 K [66], with its components exhibiting itinerant magnetism, this alloy is especially hard to model at this temperature. To treat the magnetic effects, we apply the LSF model described in Sec. II B. Following the recipes from [38], the constant a for the magnetic entropic contributions is chosen for each component based on fixed spin-moment calculations at zero temperature:

$$\text{Ni}: \quad S_{\text{mag}} = 3 \log M, \tag{10}$$

$$\text{Co}: \quad S_{\text{mag}} = 2 \log M, \tag{11}$$

$$\text{Cr}: \quad S_{\text{mag}} = 3 \log M. \tag{12}$$

We start by analyzing apparent and misfit volumes of individual components (Ni, Co, and Cr), as they are the key quantities in the VC model. The results are shown in Fig. 2, where we compare them to the experimental measurements and earlier DFT calculations from Ref. [23]. Furthermore, we show how our methodology is getting more and more accurate by gradually including finite-temperature effects and exchange-correlation corrections.

The biggest effect on the calculated equilibrium volume can be seen from using XC pressure correction, which is expected for LDA, since it is known to underestimate the volume of 3d metals considerably. It changes the equilibrium volume by more than 8% [from 10.20 Å^3 (LDA-0) to 11.03 Å^3 9XPC-0)]. Including thermal electronic and phonon

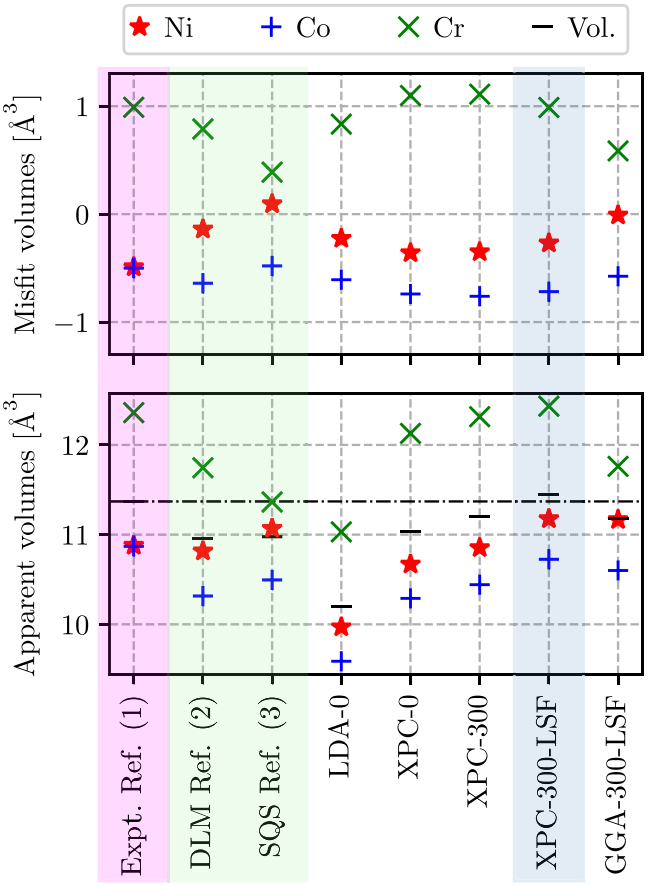

FIG. 2. Comparison of experimentally measured and calculated apparent, misfit ($\times, +, \star$) and equilibrium volumes ($-$). Dashed-dotted line indicates the experimental equilibrium volume. Ref. (1): volumes extracted from experimental measurements [23]. DLM Ref. (2): CPA-DLM calculations [23]. SQS Ref. (3): SQS calculations [23]. For our calculations, results of applying successively finite-temperature effects and exchange-correlation corrections are displayed. (LDA-0) and (XPC-0): CPA-DLM with LDA calculation at 0 K without and with applying the exchange-correlation correction. (XPC-300): Applying finite-temperature phonon contributions within the Debye-Grüneisen model at 300 K. (XPC-300-LSF): Additionally adding LSF. (GGA-300-LSF): Conventional PBE calculation combined with DLM-LSF and phonon contributions at 300 K for comparison.

contributions leads to an additional increase in volume to 11.20 Å^3. Finally, taking also the LSF contributions into account, we obtain a volume of 11.44 Å^3 (XPC-300-LSF).

One can see that XC pressure correction and finite-temperature contributions (both with and without LSF) lead to the equilibrium volume very similar to the experimental one. At the same time, the agreement with experiment of the equilibrium volume calculated using the common PBE functional (with all finite-temperature contributions included but without XPC) seems to be as good as with our LDA-XPC approach (PBE result: 11.18 Å^3). However, previous PBE results without LSF (both DLM-CPA and SQS) from Ref. [23] underestimated the equilibrium volume of the NiCoCr alloy [by about 0.4 Å^3, see Ref. (1), Ref. (2) in Fig. 2]. The observed agreement can, thus, be attributed to the well-known

overestimation of magnetic moments by the PBE functional [57], which, with the help of LSF, compensates for the error in the equilibrium volume. On the other hand, this compensation effect is not consistent and fails to reproduce the misfit and apparent volumes. In contrast to the equilibrium volume, calculated misfit and apparent volumes are more sensitive to the accuracy of the underlying methodology because they depend on concentration derivatives of the alloy volume. More precisely, any imbalance in the XC error produced for individual alloy components can lead to enhanced errors in the misfit volumes. Indeed, previous PBE calculations within DLM-CPA and SQS approaches from Ref. [23] showed considerable deviations of the misfit volumes from the ones obtained from experiment. In particular, the calculations underestimated the misfit volumes of Ni and Cr. Moreover, because of the their smaller equilibrium volume the apparent volumes of Co and Cr were lower than in experiment. In contrast, the combination of XC pressure correction and finite-temperature contributions results in a very good agreement of misfit and apparent volumes, as seen in Fig. 2 (XPC-300-LSF).

In particular, the misfit volume of Cr (0.99 Å^3) is practically the same as in experiment (0.99 Å^3), while the results for Ni and Co (misfit volumes −0.28 and −0.71 Å^3, respectively) are only slightly different from the experimental ones (−0.49 and −0.50 Å^3, respectively). Taking into account the good agreement of the equilibrium volume noted above, the apparent volumes also turn out to be close to experiment. It is clear from Fig. 2 that the success in producing good misfit volumes in this particular alloy can be largely attributed to XC pressure correction, while the finite-temperature contributions are responsible for a more accurate equilibrium volume and hence apparent volumes of components.

Next, we calculate how the SSS contribution to the yield stress evolves with temperature and compare it to experimental measurements. In Fig. 3, theoretical and experimental CRSS are compared for each of our alloys: Poly. Expt. and Sing. Expt. denote experimental values from polycrystalline and single-crystalline samples, respectively; DFT refers to the CRSS from our methodology with all material parameters being calculated for the respective temperature; 0 K DFT corresponds to our theoretical CRSS using the material parameters at 0 K, however, still considering the alloy to be paramagnetic and with the temperature dependence being determined solely by the Arrhenius-type expression from Eqs. (5) and (4). Furthermore, we also added an uncertainty estimate for the calculated CRSS (ΔDFT), which shows how differences between the predicted and experimental elastic constants, misfits, and equilibrium volume influence the final result of the CRSS. In order to get the experimental values of the CRSS from the polycrystalline measurements, we are using the Taylor factor of 3.06 to get the single-crystalline values and then subtract the grain-size-dependent contribution obtained from the Hall-Petch fit. For the case of NiCoCr, polycrystalline tensile results from Ref. [75] with a Hall-Petch contribution of 39 MPa from Ref. [23] were used.

For NiCoCr, Fig. 3(a) clearly shows that the full account of temperature dependence of the material properties results not only in qualitative but also in a very good quantitative agreement of the calculated CRSS with the experimental one, in a wide temperature range from 77 to 673 K. In contrast,

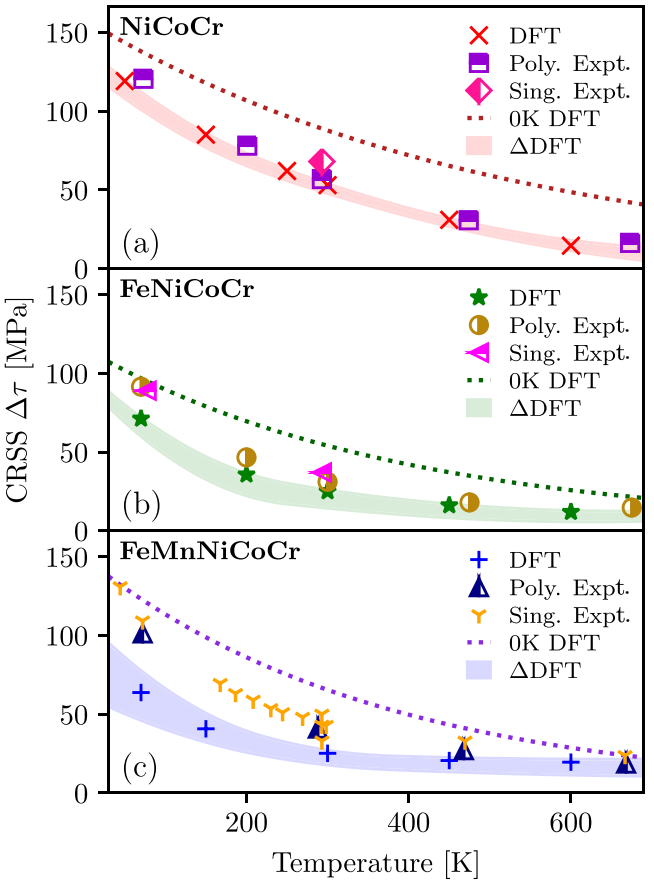

FIG. 3. Comparison of CRSS $\Delta\tau$ from calculations and experiments versus temperature of NiCoCr (a), FeNiCoCr (b), and FeMnNiCoCr (c). (Poly. Expt.): Experimental polycrystalline measurements with subtracted Hall-Petch contribution [67,68]. (Sing. Expt.): Experimental single-crystalline measurements [69–73]. (DFT): Theoretical CRSS with all material parameters calculated for the given temperature and uncertainties (filled curves) due to deviations from experiment. (DFT 0 K) (dashed lines): Theoretical CRSS with all material parameters calculated once for 0 K and then used for the whole temperature range.

using only 0-K parameters throughout the whole temperature range leads to an obviously different behavior at higher temperatures. According to Eqs. (5) and (4), the temperature dependence of the CRSS is mostly determined by the energy barrier ΔE_b, which is itself a function of the misfit volumes, elastic moduli, and volume [Eq. (7)]. As can be seen in Fig. 4(a), the misfit volumes of NiCoCr are only slightly affected by finite-temperature effects and stay almost constant up until 600 K. Together with the moderate increase of the equilibrium volume this also leads to an almost constant misfit parameter δ [Fig. 5(a)]. At the same time, the shear modulus G_V decreases linearly with temperature, as can be inferred from Fig. 5(b), where we also provide room-temperature experimental values from Ref. [74] for comparison. This softening, in turn, reduces the energy barrier ΔE_b for dislocation glide, resulting in an additional reduction of the yield stress on top of the simple thermal activation process. Note also that the CRSS is reduced even further because of decreasing τ_{0y} whose T dependence is similar to that of ΔE_b. It is also worth noting

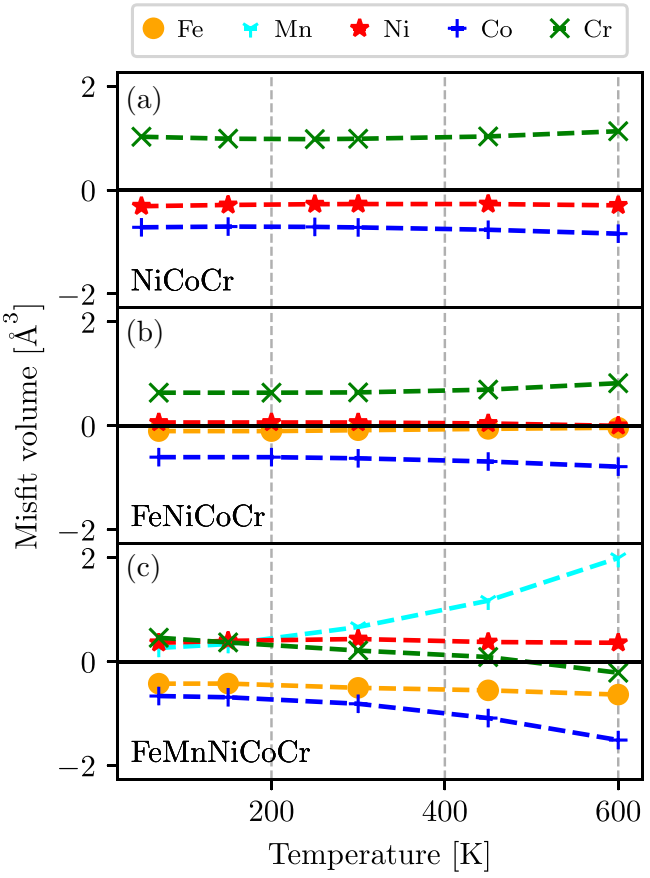

FIG. 4. Comparison of misfit volumes of the individual components for the (a) NiCoCr, (b) FeNiCoCr, and (c) FeMnNiCoCr alloy versus temperature.

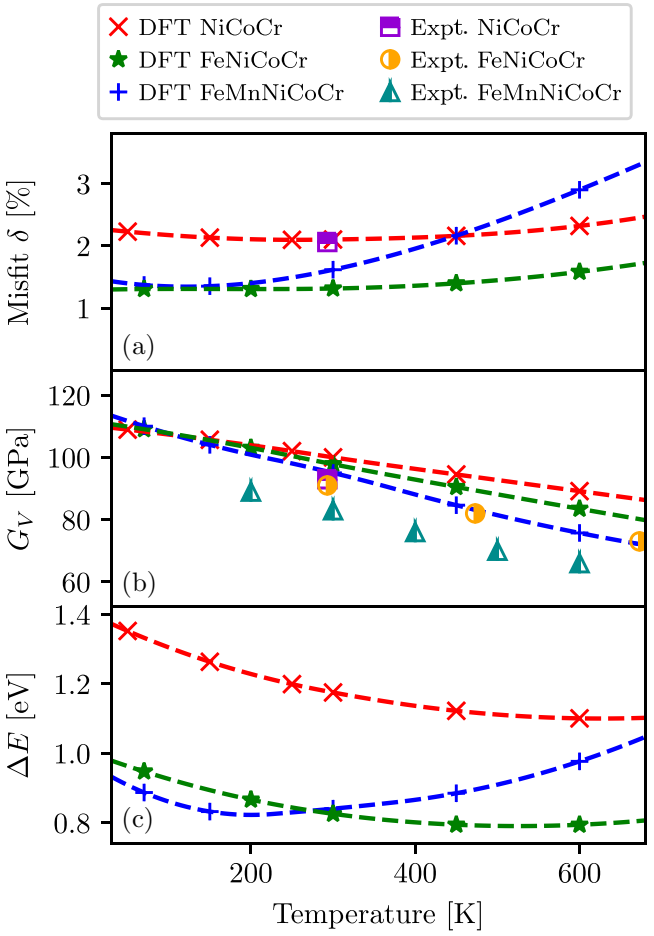

FIG. 5. Comparison of the main parameters of the VC model from calculations and experiments versus temperature of (a) NiCoCr, (b) FeNiCoCr, and (c) FeMnNiCoCr. (a) Calculated and experimental [23] misfit parameter δ. (b) Calculated Voigt-averaged shear modulus and experimental values of the shear modulus [52,74–77]. (c) Calculated results for energy barrier ΔE_b.

that the uncertainties, which are mainly stemming from the overestimated shear modulus, are rather small, with values of around 10 MPa at low temperatures (below 100 K) and around 4 MPa above room temperature (RT).

Finally, we take a closer look at the CRSS at room temperature and compare our calculated value $\Delta\tau = 63$ MPa to earlier works. Single-crystal tensile measurements in Ref. [69] yielded 69 MPa. A slightly different value of 63 MPa was found in Ref. [23] by extrapolating the Hall-Petch relation to infinite grain size and by dividing the results for polycrystalline samples by the Taylor factor. A comparable value of 59 MPa was calculated using the same VC model, with the parameters estimated from experimental data [10]. At the same time, previous *ab initio* calculations seem to have failed to predict the yield stress of NiCoCr. For instance, Liu *et al.* [78] used the Peierls model to estimate the zero-temperature CRSS to be equal to 214 MPa. This significantly overestimates our 0-K prediction of 158 MPa. Finally, Yin *et al.* [23] have obtained the CRSS at room temperature of about 19 MPa, whereby they have applied the VC model, with the parameters calculated using the PBE functional and a SQS setup for the alloy, finite-temperature contributions being neglected.

B. FeNiCoCr

FeNiCoCr is paramagnetic at room temperature [79] with a T_c of around 85 K and can be produced as a single-phase fcc alloy [67,70] without detectable long-range order [59]. However, its paramagnetic behavior differs from that of NiCoCr. Specifically, unlike Ni, Co, and Cr, the magnetic moment of Fe is strongly localized and remains significant even at zero temperature [80,81]. We, therefore, use the LSF entropy term for localized moments: $S_{\mathrm{mag}} = \log(1 + M)$ [38]. To summarize, the following magnetic entropy contributions are chosen for each component:

$$\begin{aligned} \text{Fe}: &\quad S_{\mathrm{mag}} = \log(1+M), \\ \text{Ni}: &\quad S_{\mathrm{mag}} = 3\log M, \\ \text{Co}: &\quad S_{\mathrm{mag}} = 2\log M, \\ \text{Cr}: &\quad S_{\mathrm{mag}} = 3\log M. \end{aligned}$$

As in the previous case, we have calculated all temperature points with the DLM-LSF approach. This includes also the first experimental point at 77 K that lies below the magnetic transition temperature. However, since this point is very close to $T_c = 85$ K, we expect a significant magnetic disorder, which is better described by DLM than the ferromagnetic state [82].

The results for FeNiCoCr are presented in the middle panel of Fig. 3, where again, one can see a very good agreement for the calculated $\Delta\tau(T)$ (DFT) with experimental data from Refs. [67,70]. The difference between the full (DFT) and no (0 K DFT) temperature dependence of material parameters is even more pronounced than in the NiCoCr alloy, where the latter fails to reproduce the significant drop in strength below RT. It is also clear that the CRSS turns out to be considerably lower than in NiCoCr. To analyze this difference, we examine individual contributions to the value of $\Delta\tau$.

The calculated Voigt-averaged shear modulus G_V is displayed in the middle panel of Fig. 3 along with experimental values from Ref. [75] for comparison. The value of G_V is similar to that of NiCoCr, with a slightly more enhanced softening with temperature. As already seen in the analysis of the uncertainties, small differences in the shear modulus between the two alloys cannot explain the much stronger difference in the CRSS. The equilibrium volume of FeNiCoCr at room temperature, 11.32 Å^3 [59], is practically the same as that of NiCoCr. Our equilibrium volume of 11.44 Å^3 calculated at room temperature also agrees quite well with this experimental value.

Next, we consider the misfit volumes of alloy components [Fig. 4(b)] and the average misfit parameter δ [Fig. 5(a)]. Despite having almost the same equilibrium volume as NiCoCr, the misfit volumes of Ni, Co, and Cr components in FeNiCoCr differ significantly from those in the ternary system. While the order has remained the same ($\Delta V_{\mathrm{Co}} < \Delta V_{\mathrm{Ni}} < \Delta V_{\mathrm{Cr}}$), the difference between the smallest (Co) and the largest (Cr) components in FeNiCoCr at RT is 1.27 Å^3, which is 25% smaller than in NiCoCr, where the difference between Co and Cr is 1.7 Å^3 (see previous subsection). On the other hand, Ni and Fe have negligible contributions to the average misfit δ in FeNiCoCr. The net effect is the reduction of δ from 2.1% in NiCoCr to 1.6% in FeNiCoCr, which has the largest impact on the final values of $\Delta\tau(T)$. The consequently lower-energy barrier ΔE_b causes the CRSS to fall off significantly below RT [Fig. 3(b)]. The T dependence of the misfit volumes and hence of the average misfit δ in FeNiCoCr is practically absent below the RT and remains relatively weak at higher temperatures up until 673 K.

We can also compare our calculated CRSS to other experimental data measured at selected temperatures. Single-crystalline CRSS measurements from Wu *et al.* [70] yielded $\Delta\tau = 89$ MPa for 77 K and 39 MPa for RT. For the same temperatures, the extrapolated polycrystalline CRSS from Ref. [67] are 95 and 30 MPa, respectively. This is to be compared to our calculated values for the same two temperatures: 77 and 25 MPa, respectively.

C. FeMnNiCoCr

As a third example, we consider solid solutions of FeMnNiCoCr whose equimolar composition is known as the Cantor alloy, for which we also study the effect of concentration variations. A wide range of compositions of FeMnNiCoCr systems were studied, with their microstructure being claimed to be a single-phase fcc solid solution [21,83,84]. This makes it especially interesting as a playground for property optimization. FeMnNiCoCr is paramagnetic at room temperature, with T_c being around 38 K [85]. The magnetic moments of Mn show localized behavior with a nonvanishing moment at zero temperature [80,81] similar to Fe. The following magnetic entropy contributions are chosen for each component:

$$\begin{aligned}
\text{Fe}: &\quad S_{\mathrm{mag}} = \log(1+M),\\
\text{Mn}: &\quad S_{\mathrm{mag}} = \log(1+M),\\
\text{Ni}: &\quad S_{\mathrm{mag}} = 3\,\log M,\\
\text{Co}: &\quad S_{\mathrm{mag}} = 3\,\log M,\\
\text{Cr}: &\quad S_{\mathrm{mag}} = 3\,\log M.
\end{aligned}$$

From the results presented in Fig. 3, one can immediately see that the behavior of the Cantor alloy is generally more involved than in the two previous cases. First of all, we see that the calculated CRSS has an appreciably weaker temperature dependence than in NiCoCr and FeNiCoCr. The CRSS at RT is practically the same (26 MPa) as in FeNiCoCr despite being significantly smaller at lower temperatures. The more so, our calculations seem to systematically underestimate the CRSS compared to experiment [68,75]. Especially at lower temperatures, we see differences of more than 30 MPa. Before discussing possible reasons for such a discrepancy, let us analyze the behavior of the alloy in more details.

First, the addition of Mn results in the increase of the equilibrium volume compared to NiCoCr and FeNiCoCr, with the calculated volume being 11.62 Å^3 at RT, which nicely compares to the experimental value 11.56 Å^3 [58]. On the other hand, the shear modulus is only marginally smaller than in FeNiCoCr with the RT value for G_V being 95 GPa. Overall, the calculated shear modulus as function of temperature is somewhat larger compared to experimental values from Ref. [76], as can be seen in Fig. 5(b). Temperature-induced softening is slightly more pronounced as compared to the previous two alloys. The anti-invar behavior poses a problem for the precise and unambiguous determination of the bulk modulus. As a result, a comparably large uncertainty in CRSS $\Delta\tau$ arises [ΔDFT in Fig. 3(c)].

The apparent volumes of Co, Cr, and Fe at RT are similar to those of FeNiCoCr causing the misfit volumes to be just shifted because of the difference in equilibrium volumes [Fig. 4(c)]. Ni appears to be even larger than Cr in the Cantor alloy, making it a significant strengthener in contrast to the other two alloys. Compared to the previous two cases, the misfit volumes of the Cantor alloy exhibit a significant temperature dependence above RT with Mn being most strongly affected. At low temperatures, the previously found order of misfit volumes is retained, with Co being the smallest, followed by Fe, Ni, and Cr. Mn lies in-between Ni and Cr. At 600 K, however, Mn has by far the largest apparent volume and Ni and Cr are switching places, with Ni becoming larger than Cr. Starting from a value of 0.67 at RT, the misfit volume of Mn reaches a value of 2.00 at 600 K. Combined with the decreasing misfit volumes of Cr and Co, this leads to an effective doubling of misfit parameter δ from RT to 600 K. This compensates for the effect of elastic softening, giving rise to both the energy barrier ΔE_b and the zero-temperature yield strength τ_{y0} to gradually increase again starting from RT. This, finally, results in a plateau in the T dependence of $\Delta\tau$ above RT.

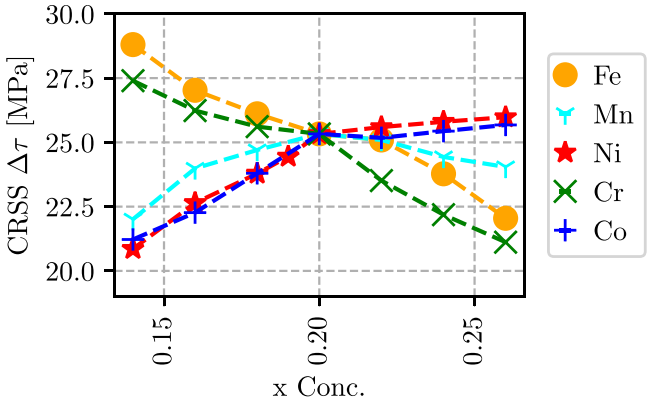

FIG. 6. CRSS $\Delta\tau$ of nonequimolar FeMnNiCoCr Cantor alloys with varying concentrations. x denotes the concentration of the component that is varied, while the remaining component concentrations are kept equimolar.

Next, we take a closer look at how our theoretical findings of CRSS compare with the available experimental data. At RT, the yield stress ranges from 33–50 MPa [71–73] (single-crystal results) to 49–55 MPa [2,68] (extrapolated polycrystalline data), which is above our calculated value of 26 MPa. For 77 K we get 67 MPa compared to 105 MPa [73] and 100 MPa [68], which indicates a considerable underestimation, even when the calculation uncertainty of 15 MPa is taken into account. The discrepancy can be attributed to a likely deviation of the structure of the Cantor alloy from the idealized solid solution assumed in the calculations. Specifically, the five-component system has a strong tendency to phase separation observed in multiple experiments [2,86–88]. On top of that, even a single phase of a HEA can experience partial ordering or clustering on individual sublattices, which would appear as a homogeneous phase and could be detected only by experimental techniques capable of resolving a homogeneous short-range order [89].

To further investigate the complex interplay of the Cantor alloy components and to understand its behavior better, we also study the CRSS as a function of concentrations of components in the vicinity of the equimolar composition. In particular, we always vary one component concentration, while keeping the composition of the remaining system equimolar. Figure 6 summarizes the CRSS for all component variations. Judging by the misfit volumes of the equimolar composition, one would expect that increasing the concentration of elements with large absolute misfit volumes, such as Mn and Cr, would also positively affect the CRSS. Surprisingly, the result for Mn and Cr is the opposite, while increasing the concentrations of Co turns out to be marginally beneficial for the strength. By examining the behavior of individual contributions (see Appendix B), we conclude that for Mn the outcome is related to considerable softening of elastic constants, compensating the increasing misfit parameter δ. At the same time, both the shear modulus and the misfit parameter are decreasing with concentration of Cr, resulting in the reduced CRSS. On the other hand, lowering the Fe content increases δ, while reducing the elastic constants only moderately, which gives rise to a positive impact on the CRSS. This counterintuitive behavior of the CRSS is the result of complex interactions between the components. We will discuss these interactions in more details in the next section.

IV. DISCUSSION

Naturally, one would expect that a higher number of elements would enhance solid solution strengthening and ultimately lead to a higher yield stress. However, previous experimental work of tensile tests of polycrystalline samples yield strength measurements on single-crystal and hardness measurements show a different trend for the NiCoCr, FeNiCoCr, and FeMnNiCoCr alloys [67,90]. Specifically, it is the ternary NiCoCr that has the highest SSS contribution, while the five-component Cantor and the quaternary FeNiCoCr alloy have almost the same SSS, with the latter having the lowest value. At the same time, specific volume and linear elastic constants are very similar for these alloys, which leaves the average misfit volume as a parameter of the VC model mainly responsible for the differences in the SSS. Results presented in the previous section show that that our theoretical findings confirm the trends observed in experiments. In particular, NiCoCr has the largest SSS, with the four- and five-component alloys having considerably lower effect of solutes on strengthening.

Modeling also confirms that the differences between the alloys clearly correlate with the magnitude of the average misfit volumes. We can therefore understand the mechanism of strengthening better by analyzing the behavior of misfit volumes. Since direct measurements of misfit/apparent volumes are relatively difficult, they are often estimated from measured volumes of a set of simpler alloys containing corresponding elements, whereby a linear dependence of the alloy volume on concentrations (Zen-Vegard's law [91]) is assumed. Apparent volumes obtained in this way for iron-group $3d$ metals usually follow the order similar to the well-known trend followed by the corresponding elemental compounds [10,11,21]. Specifically, starting from Ni and going down the row, the volume steadily increases, reaching its maximum at Mn and then slightly decreasing for Cr. However, our calculations suggest that the apparent volumes are strongly system dependent and generally do not follow the naive elemental trend. For instance, for all three alloys considered in this work, Ni is never the smallest element and exhibits even a larger volume than that of Cr in the five-component Cantor alloy (see Appendix B). Furthermore, previous works suggested that the average misfit δ is increasing for FeNiCoCr, NiCoCr, and FeMnNiCoCr (respectively, values of 1.72%, 1.67%, 1.85% were obtained in Ref. [11] and 1.24%, 1.07%, 1.89% in Ref. [21]), while our results clearly show that it is NiCoCr that has the largest average misfit volume among these three alloys (with the RT value of 2.1% compared with 1.31% and 1.61% for FeNiCoCr and FeMnNiCoCr, respectively).

The failure of the simple Vegard's law in predicting the misfit volumes can be attributed to two main phenomena. First, the magnetic behavior of the iron-group elements is pretty complex and has a considerable influence on the misfit volumes. In particular, Fe and especially Mn exhibit strong magnetovolume coupling, which effectively makes their local magnetic moments dependent on their respective

apparent volumes. Second, chemical and magnetic interactions between components in multicomponent HEA lead to appreciable deviations of the concentration dependence of the volume from Vegard's law.

Because of magnetism, formulating a tractable general model for predicting misfit volumes is a nontrivial task. Nevertheless, basic aspects of interatomic interactions beyond Vegard's law can be rationalized within a relatively simple framework that we will present below. The behavior of volumes in a multicomponent alloy is best inferred from the Gibbs free energy of a system $G(T, P, \{c_i\})$, which is a function of temperature T, pressure P, and concentrations of components c_i. Once the Gibbs free energy is known, the concentration-dependent volume of the alloy for a given temperature (which we will omit for clarity) is readily obtained as

$$V(\{c_i\}) = \frac{\partial G(P, \{c_i\})}{\partial P}, \tag{13}$$

which is then used to evaluate misfit volumes according to Eq. (9).

A standard way to analyze the free energy would be to use the cluster expansion, which for a completely random alloy of n components can be written as a series over powers of concentrations,

$$G(P, \{c_i\}) = \sum_{k=1}^{\infty} \sum_{p_1 p_2 \dots p_n} g^{(k)}_{p_1 p_2 \dots p_n}(P) c_1^{p_1} c_2^{p_2} \dots c_n^{p_n}, \tag{14}$$

where $g^{(k)}_{p_1 p_2 \dots p_n}(P)$ are effective intercomponent interactions of kth order, with $p_1 + p_2 + \dots + p_n = k$. The interactions depend only on the pressure and component types and can formally be obtained as a sum over corresponding cluster interactions. However, this series is generally slowly convergent in the order of interactions, making it impractical for a model description. The situation gets worse in magnetic alloys, where magnetic interactions and the concentration dependence of local magnetic moments of components render the above series even slower convergent (or not convergent at all).

A much more compact description can be obtained if we introduce two major assumptions: (i) effective interactions $g^{(k)}$ can be made explicitly dependent on the local magnetic moments of the components m_i; (ii) given the local magnetic moments, effective interactions depend on the component types only through the average number of d electrons per k-site cluster, $N^{(k)} = (p_1 N_1 + \dots + p_k N_k)/k$, with N_i being the number of d electrons for component i. This approximation is known as a virtual bond approximation (VBA) [92] and its idea is to reduce complex intercomponent interactions to simpler universal (virtual bond) functions of the average valence in the spirit of the Pettifor theory of bonding in transition metals [93]. Virtual bond parameters can also be loosely connected to tight-binding bond order parameters, which reflect the dependence of the bond energy on electron filling [94]. Another similar approach is a model proposed in Ref. [95], which expresses the alloy lattice parameter in terms of a second-order polynomial in concentrations. Within the VBA model, Gibbs free energy and the equilibrium volume of an alloy can be written as

$$G(P, \{c_i\}) = \sum_i c_i g^{(1)}(P, N_i, m_i) + \sum_{ij} c_i c_j g^{(2)}(P, N_{ij}, m_i, m_j) + \dots, \tag{15}$$

$$V(\{c_i\}) = \sum_i c_i \, v^{(1)}(N_i, m_i) + \sum_{ij} c_i \, c_j \, v^{(2)}(N_{ij}, m_i, m_j) + \dots, \tag{16}$$

where $v^{(k)} = \partial g^{(k)}(P = 0)/\partial P$, $N_{ij} = (N_i + N_j)/2$. Note that i and j can stand for the same element. In particular, the equilibrium volume of an element i will be given by $V_i = v^{(1)}[N_i] + v^{(2)}[N_{ii}]$ with $N_{ii} \equiv N_i$. The expansion can be written up to an arbitrary order but we will limit ourselves to the second order.

To determine the unknown interaction parameters $v^{(k)}$, we perform a series of calculations of equilibrium volume for equimolar binary alloys containing all possible combinations of 5 elements, Cr, Mn, Fe, Ni, Co (10 binary alloys in total). Combined with 5 elemental compounds, this gives 15 reference systems in total. Importantly, the calculations are performed with the local moments m_i fixed to that of the target alloy. Also, their structure is considered to be the same as the target. In practice, we fix the local moments to those of the Cantor alloy since their values in NiCoCr and FeNiCoCr are not significantly different. Since the model is linear in interaction parameters $v^{(k)}$, one way to find them would be to perform a linear regression on the entire set of reference systems. However, one can simplify the fitting procedure by noticing that the model with second-order terms ($v^{(2)}$) omitted is equivalent to Vegard's law, with $v^{(1)}$ just being the simple elemental equilibrium volume. Any deviation from Vegard's law, $\Delta V = V_{\text{alloy}} - \langle V \rangle$, will thus be determined solely by interaction terms $v^{(2)}$. In more details, for an equimolar binary AB the deviation $\Delta V_{AB} = V_{AB} - \langle V \rangle_{AB}$ is given by

$$\Delta V_{AB} = \tfrac{1}{2} v^{(2)}[N_{AB}] - \tfrac{1}{4} v^{(2)}[N_A] - \tfrac{1}{4} v^{(2)}[N_B], \tag{17}$$

which results in a (generally overdetermined) system of equations in terms of parameters $v^{(2)}$, with ΔV_{AB} obtained from the calculated equilibrium volumes of the binary alloys. Subsequently, $v^{(1)}$ is obtained trivially from the equilibrium volumes of reference systems using Eq. (16). If the model consistently describes the reference systems we expect parameters $v^{(k)}$ to come out as smooth functions of the valence. This is indeed the case, as one can see in Fig. 7, where we show that the obtained parameter values can be fitted with low-order polynomials. It is also clear that although the volume is dominated by the first-order parameter $v^{(1)}$, the variation of $v^{(2)}$ is significant and it can result in nontrivial contributions to the equilibrium volume and its concentration derivatives for multicomponent alloys.

Misfit volumes derived from Vegard's law and the VBA model for the three alloys, NiCoCr, FeNiCoCr, FeMnNiCoCr, are displayed in Fig. 8, where they are compared to the calculated values (denoted by "C"). To get the model estimates we use the polynomial fits of $v^{(1)}$ and $v^{(2)}$ as functions of

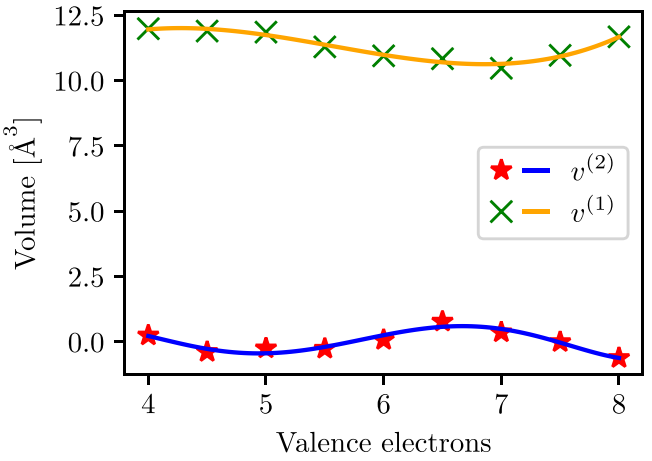

FIG. 7. VBA parameters $v^{(1)}$ and $v^{(2)}$ as functions of the average number of d-valence electrons. Discrete values ($\times$, $*$) were obtained from equilibrium volumes of elemental compounds and binary alloys as described in the main text. Solid lines are polynomial fits (third order for $v^{(1)}$ and fifth order for $v^{(2)}$).

the valence, which allows us to evaluate these parameters at an arbitrary value of the d-electron filling. Furthermore, we use either nominal valences of elements ("M1" in the figure) or the actual fillings including charge transfers ("M2" in the figure) obtained from the calculations. From Fig. 8 one can see that the naive Vegard's law ("V") works fairly well only for NiCoCr, while failing completely to reproduce the signs and relative sizes of calculated misfit volumes in FeNiCoCr and FeMnNiCoCr. In the latter case, even the order of elements turns out to be wrong with a strongly overestimated value for Cr and underestimated values for Ni and Mn. The reason for this failure is clear: Since the volumes of the three alloys are very similar, the obtained misfit volumes simply follow the trend for the volumes of 3d elements. However,

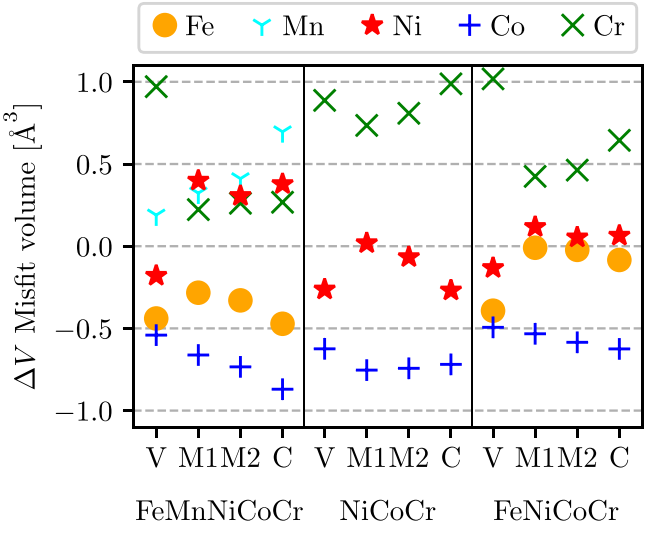

FIG. 8. Comparison of the misfit volumes obtained from Vegard's law (V), from virtual bond approximation with nominal valences (M1), with charge transfers taken into account (M2), and calculated directly (C).

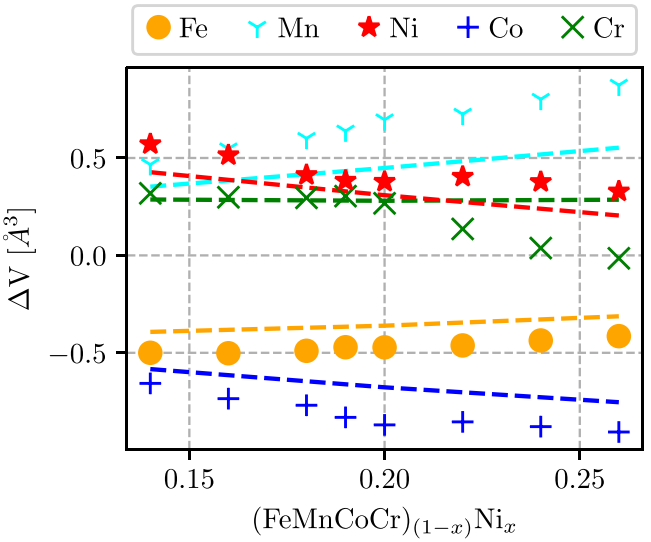

FIG. 9. Comparison of the directly calculated and model predictions of misfit volume of the Cantor alloy for concentration variations of Ni.

we have seen already that the misfit volumes in the four- and five-component alloys deviate considerably from this trend.

In contrast, misfit volumes from the VBA (M1 and M2) exhibit much better agreement with calculations. In particular, the signs are always correct and values are mostly in the right ballpark. The order of the elements is also generally correct except for the significant underestimation of Mn misfit volume in the Cantor alloy by the simpler version (M1) of the model. However, this error is mitigated if one takes charge transfer into account (M2), which gives an overall better agreement in all cases. The considerable improvement of the VBA misfit volumes over those from Vegard's law signify the importance of including intercomponent interactions into the model.

Another important feature of the VBA model is that it can be used to predict the evolution of the misfit volumes when the composition of a HEA is varied away from the equimolar point. An example is shown in Fig. 9, where the VBA misfit volumes are compared to the calculated ones as functions of the concentration of Ni in the Cantor alloy while keeping the other components equimolar. As expected from the second-order model, it can result only in a linear dependence on the concentration. The concentration dependence of the local magnetic moments is ignored here. Including changes in the d fillings with concentration have a weak effect. Nevertheless, most of the trends are correctly reproduced. In contrast, Vegard's law would give values shifting uniformly in the same direction with composition only because of the variation of the equilibrium volume itself.

The presented model could, in principle, be used for predicting misfit volumes of HEA based on experimental data on binary and ternary subsystems. However, the inference of parameters $v^{(k)}$ for iron-group HEA is complicated by the complex magnetic behavior of elements, especially Mn and Fe. In particular, one would need an additional model to predict the local moments of components and to take into account their effect on $v^{(k)}$. These issues will be addressed in future publications.

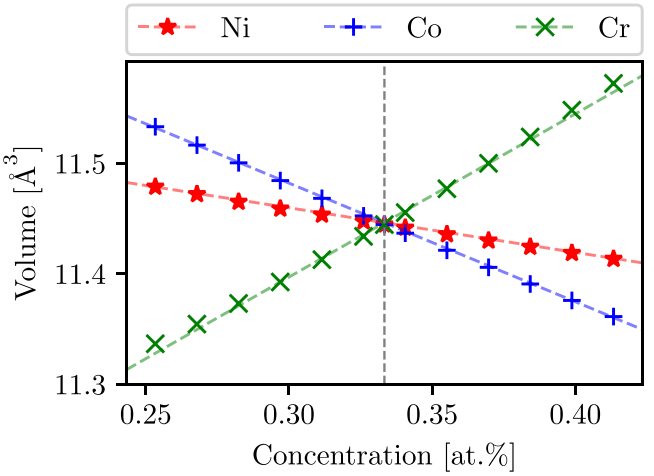

FIG. 10. Atomic volumes calculated for different concentration variation of the NiCoCr alloy used for obtaining misfit volumes. The label Ni (red), Co (blue), or Cr (green) refers to the elemental component which concentration is varied, while the other two component concentration ratios are kept constant. The markers refer to volumes obtained with our methodology. The lines correspond to a linear hyperplane fitted with the volumes. Ni and Co show a linear trend over a the large concentration range. Cr is starting to deviate for concentration changes larger than 3 at.%.

V. CONCLUSIONS

We have shown that a quite reliable description of such a complex alloy property as the critical resolved shear stress is possible using DFT combined with CPA, provided that (a) the equilibrium volume is estimated correctly, and (b) important finite-temperature effects, such as the thermal expansion and spin fluctuations, are taken into account. An accurate value of the equilibrium volume is obtained using an element-specific XC pressure correction, which is a key feature of our approach. The improved equilibrium volume also leads to significantly more accurate results for other equilibrium properties, such as elastic constants, magnetic moments, etc. Furthermore, temperature effects mediated by phonons and magnetic fluctuations are taken into account, which allows us to predict the behavior of alloys at finite temperatures.

We validate the computational approach against available experimental data for a series of alloys. In particular, we have obtained a very good estimate of the misfit volumes in the case of NiCoCr, where we can juxtapose them with the corresponding experimental data. The methodology is applied to modeling of solid solution strengthening. Specifically, we have calculated alloy-specific parameters (lattice constant, misfit parameter, elastic moduli) at respective temperatures and employed the Varvenne-Curtin model to evaluate the temperature-dependent CRSS for three alloys (NiCoCr, FeNiCoCr, FeMnNiCoCr) for which corresponding experimental data are available. We get a good quantitative agreement for the temperature-dependent CRSS for NiCoCr and FeNiCoCr. For the five-component system we get somewhat underestimated values, which we attribute to the complexity of the alloy structure. We have shown that the trends in the strength of the three alloys in question are mostly determined by the misfit parameter δ. By examining

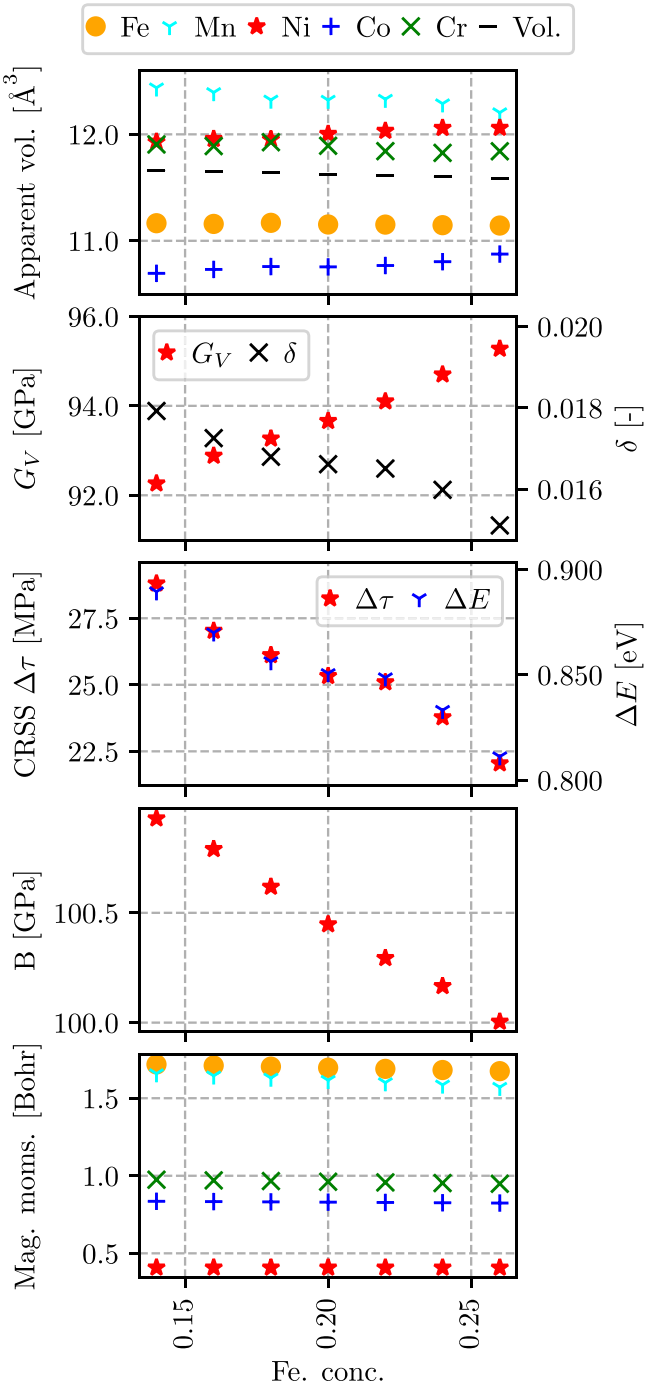

FIG. 11. Effects on properties upon changing the concentration x in $Fe_xMn_{(1-x)/4}Ni_{(1-x)/4}Cr_{(1-x)/4}Co_{(1-x)/4}$.

the contributions of individual elements into the average misfit parameter, we conclude that misfit volumes are subject to intricate intercomponent interactions and can behave in a nonintuitive way as functions of concentrations.

Finally, to examine complex interaction effects we propose a simple model describing local bond strength between individual elements. The model yields qualitatively good estimates of misfit volumes of individual components, describing the differences in the behavior of the three considered alloys. Moreover, the model is capable of capturing trends in the

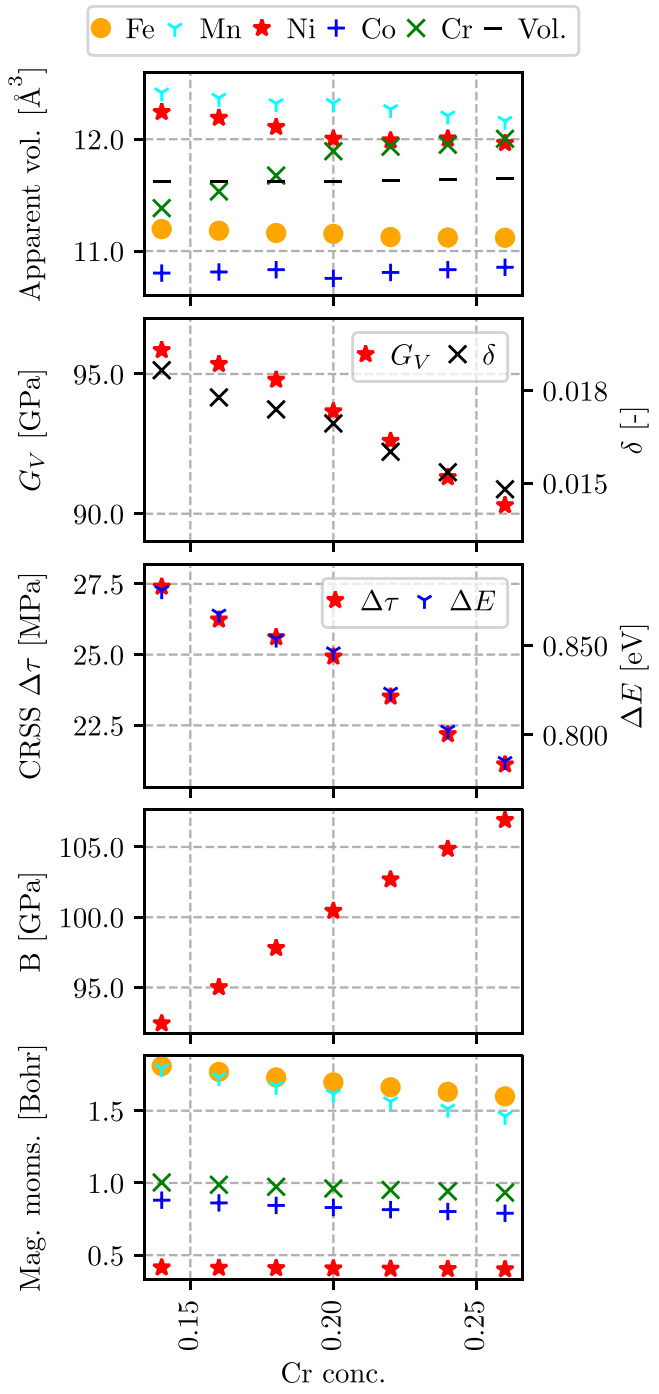

FIG. 12. Effects on properties upon changing the concentration x in $Fe_{(1-x)/4}Mn_{(1-x)/4}Ni_{(1-x)/4}Cr_xCo_{(1-x)/4}$.

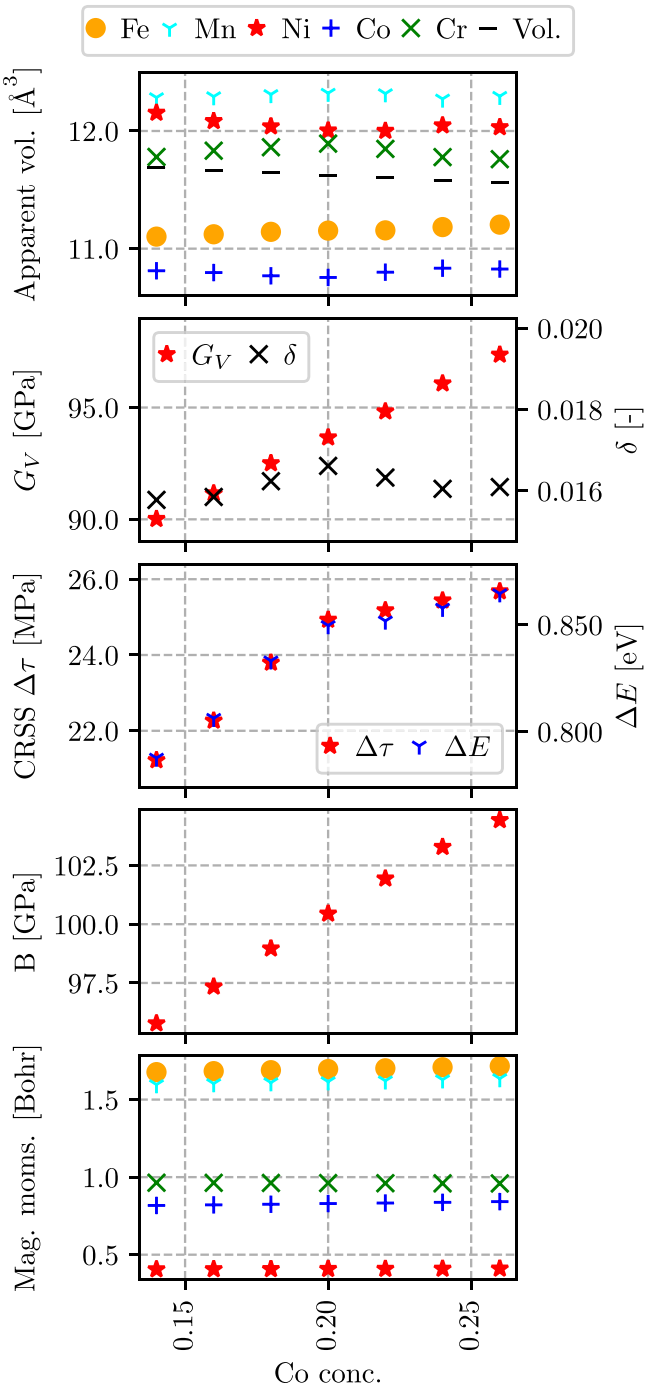

FIG. 13. Effects on properties upon changing the concentration x in $Fe_{(1-x)/4}Mn_{(1-x)/4}Ni_{(1-x)/4}Cr_{(1-x)/4}Co_x$.

evolution of misfit volumes as functions of concentrations in the FeMnNiCoCr alloy. We argue that the model could potentially be used in conjunction with available experimental data on 3*d*-metal alloys, provided that the description of magnetism is improved.

ACKNOWLEDGMENTS

We are grateful to V. Razumovskiy for discussions. This work was supported by the Forschungsförderungsgesellschaft (FFG) Project No. 878968 "ADAMANT," Austrian Science Fond (FWF) Project No. P33491-N "ReCALL," and COMET program IC-MPPE (Project No. 859480). This program is supported by the Austrian Federal Ministries for Climate Action, Environment, Energy, Mobility, Innovation and Technology (BMK) and for Digital and Economic Affairs (BMDW), represented by the Austrian research funding association (FFG), and the federal states of Styria, Upper Austria, and Tyrol. All calculations in this work have been done using Vienna Scientific Cluster (VSC-3).

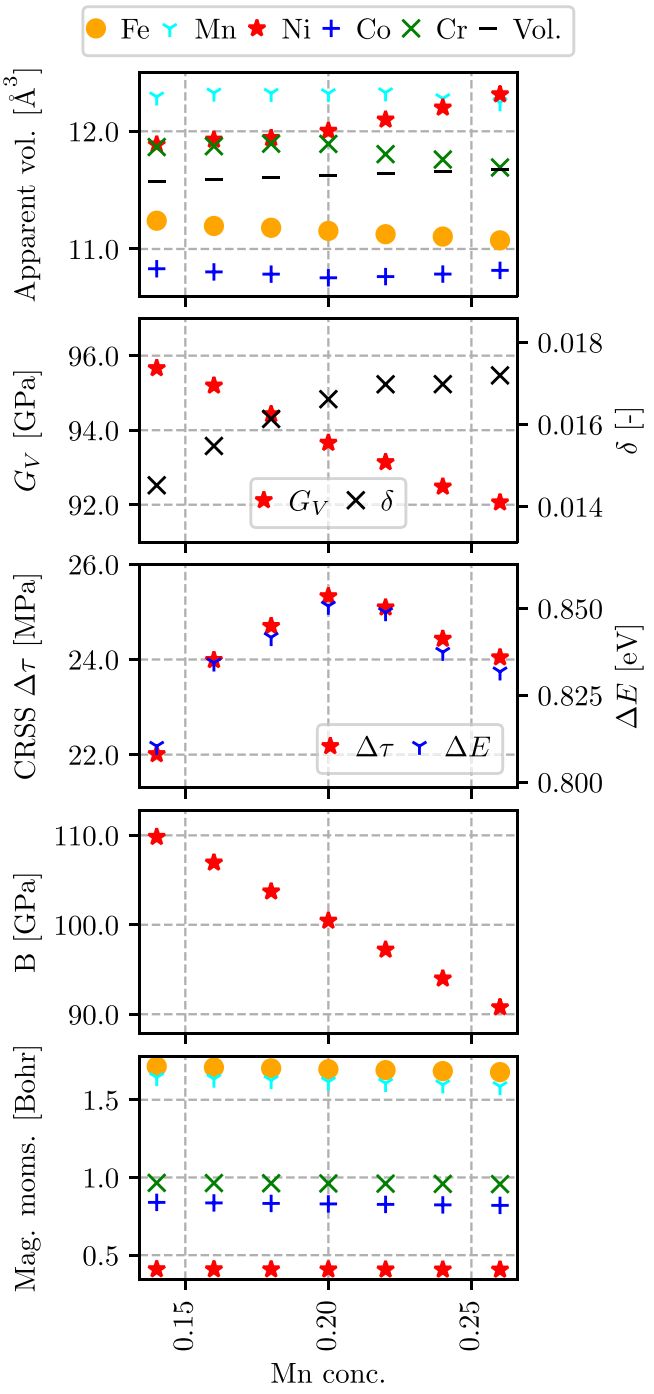

FIG. 14. Effects on properties upon changing the concentration x in $Fe_{(1-x)/4}Mn_xNi_{(1-x)/4}Cr_{(1-x)/4}Co_{(1-x)/4}$.

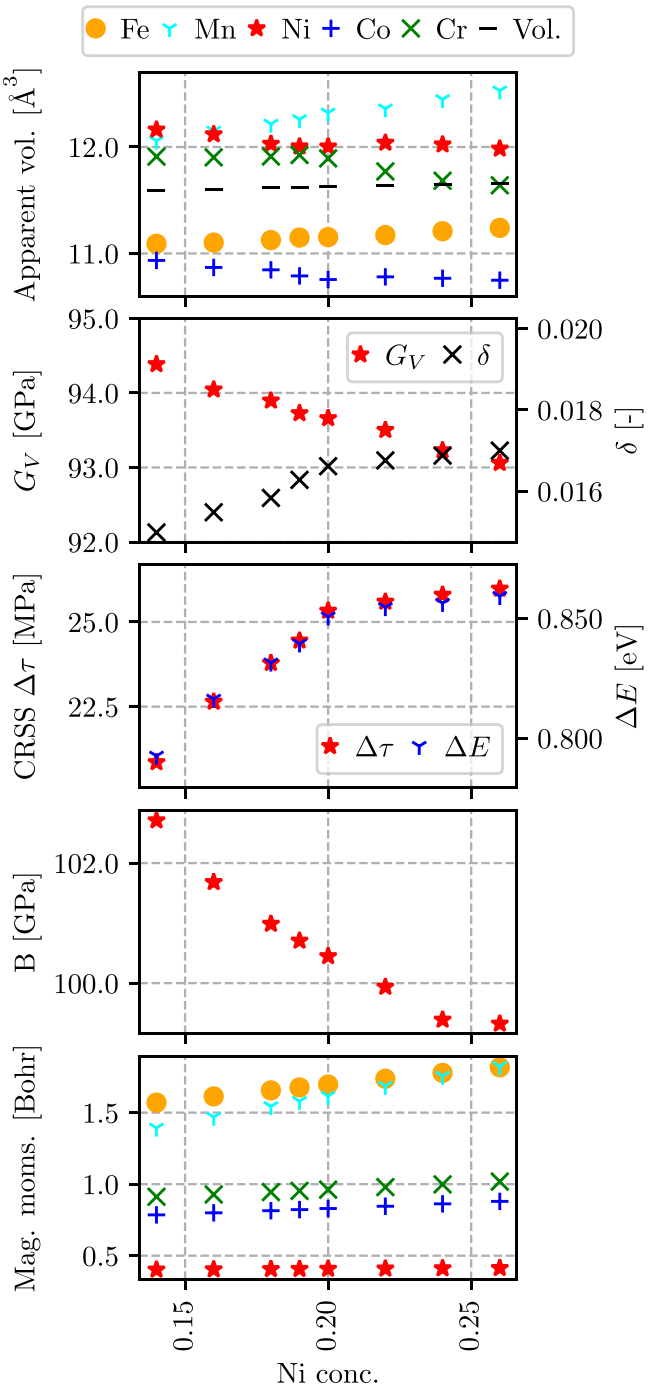

FIG. 15. Effects on properties upon changing the concentration x in $Fe_{(1-x)/4}Mn_{(1-x)/4}Ni_xCr_{(1-x)/4}Co_{(1-x)/4}$.

APPENDIX A: CONVERGENCE OF MISFIT VOLUMES

To see how sensitive our approach is to the variation of the mesh resolution, we also perform convergence tests for the concentration steps used to obtain the misfit volumes (a figure is enclosed in this Appendix). We found that convergence is achieved already with a concentration step as large as 5 at.% validating the mesh used in experiment from Ref. [23]. Specifically, NiCoCr exhibits a large linear concentration dependence of the equilibrium volumes. Often, the apparent and misfit volumes are calculated under the assumption of linearity of the average properties with respect to composition within a range of 5–10 at.% (local Vegard's law) [11,21,22,33]. Our findings generally confirm this assumption, but also demonstrate that these previous studies were choosing meshes that had already been at the limit where noticeable non-linearity starts to set in. It is worth noting that misfit volumes not only affect the yield stress at 0 K, but also its temperature dependence, which can explain, for instance,

the underestimated SSS at elevated temperatures in Ref. [33], resulting from underestimated misfit volumes.

As aforementioned, the misfit volumes require the determination of the concentration dependency of the equilibrium volumes of the respective alloy. For the NiCoCr linear dependency of the concentration is present for a large concentration range. Figure 10 depicts the changes on the volume on varying always one component while the ratio of the other two is kept constant. Changing the concentration of Ni and Co leads to a linear behavior over the whole range, as can be seen by comparing to lines representing a linear fit. In contrast, Cr shows deviations starting from concentration changes larger than 5 at.%. Overall, the deviations are small for this type of alloy.

APPENDIX B: CONCENTRATION VARIATION AROUND THE EQUIMOLAR COMPOSITION OF CANTOR ALLOY

Figures 11–15 give an overview of the influence of concentration changes on the elastic properties and apparent volumes. In all cases, one alloy component is changed with respect to the equimolar Cantor while the ratios of the remaining components are kept constant. The following properties can be seen in the overview figures: (1) apparent volume and the corresponding equilibrium volume of the alloy, (2) Voigt averages shear modulus G_V and the average misfit delta δ, (3) critical resolved shear stress at 300 K and the energy barrier, (4) bulk modulus, and (5) magnetic moments of the components at the equilibrium volume.

Several interesting observations can be made in the figures. Changes in the apparent volumes of Fe and Co are relatively weak compared to other elements, except for the case of the varying Ni concentration, where all elements are effected. Another counterintuitive aspect is that in many cases (except for Cr) the variation of an element concentration has less impact on its own apparent volume than on the apparent volume of other elements. For instance, varying Fe concentration changes the apparent volumes of Mn, Ni, and Co, but its own apparent volume remains practically constant.

One could expect that most of these variations are related to the changes in the local magnetic moment. However, the figures (bottom panels) show that the magnetic moments evolve significantly only in the case of varying Ni and Cr concentrations. And, even in these cases, it is only the variations of concentrations of Fe and Mn that can be attributed to the well-known magnetovolume coupling inherent to these elements in the fcc lattice. In all other cases, the results can be explained only taking into account intercomponent (pair or higher-order) interactions.

[1] H. S. Oh, S. J. Kim, K. Odbadrakh, W. H. Ryu, K. N. Yoon, S. Mu, F. Körmann, Y. Ikeda, C. C. Tasan, D. Raabe, T. Egami, and E. S. Park, Engineering atomic-level complexity in high-entropy and complex concentrated alloys, Nat. Commun. **10**, 2090 (2019).

[2] E. P. George, D. Raabe, and R. O. Ritchie, High-entropy alloys, Nat. Rev. Mater. **4**, 515 (2019).

[3] B. Cantor, Multicomponent and high entropy alloys, Entropy **16**, 4749 (2014).

[4] W. Steurer, Single-phase high-entropy alloys – a critical update, Mater. Charact. **162**, 110179 (2020).

[5] B. Schuh, F. Mendez-Martin, B. Völker, E. George, H. Clemens, R. Pippan, and A. Hohenwarter, Mechanical properties, microstructure and thermal stability of a nanocrystalline CoCrFeMnNi high-entropy alloy after severe plastic deformation, Acta Mater. **96**, 258 (2015).

[6] Z. Li, K. G. Pradeep, Y. Deng, D. Raabe, and C. C. Tasan, Metastable high-entropy dual-phase alloys overcome the strength–ductility trade-off, Nature (London) **534**, 227 (2016).

[7] V. Yamakov, D. Wolf, M. Salazar, S. Phillpot, and H. Gleiter, Length-scale effects in the nucleation of extended dislocations in nanocrystalline Al by molecular-dynamics simulation, Acta Mater. **49**, 2713 (2001).

[8] J. Chang, W. Cai, V. V. Bulatov, and S. Yip, Molecular dynamics simulations of motion of edge and screw dislocations in a metal, Comput. Mater. Sci. **23**, 111 (2002).

[9] D. L. Olmsted, L. G. Hector, Jr, and W. Curtin, Molecular dynamics study of solute strengthening in Al/Mg alloys, J. Mech. Phys. Solids **54**, 1763 (2006).

[10] C. Varvenne, A. Luque, and W. A. Curtin, Theory of strengthening in fcc high entropy alloys, Acta Mater. **118**, 164 (2016).

[11] C. Varvenne, G. Leyson, M. Ghazisaeidi, and W. Curtin, Solute strengthening in random alloys, Acta Mater. **124**, 660 (2017).

[12] R. L. Fleischer, Substitutional solution hardening, Acta Metall. **11**, 203 (1963).

[13] R. Labusch, A statistical theory of solid solution hardening, Phys. Status Solidi B **41**, 659 (1970).

[14] F. Nabarro, The theory of solution hardening, Philos. Mag. **35**, 613 (1977).

[15] I. Basu and J. T. D. Hosson, Strengthening mechanisms in high entropy alloys: Fundamental issues, Scr. Mater. **187**, 148 (2020).

[16] M. Yao, K. G. Pradeep, C. C. Tasan, and D. Raabe, A novel, single phase, non-equiatomic FeMnNiCoCr high-entropy alloy with exceptional phase stability and tensile ductility, Scr. Mater. **72-73**, 5 (2014).

[17] K. Pradeep, C. Tasan, M. Yao, Y. Deng, H. Springer, and D. Raabe, Non-equiatomic high entropy alloys: Approach towards rapid alloy screening and property-oriented design, Materials Science and Engineering: A **648**, 183 (2015).

[18] C. Varvenne and W. A. Curtin, Strengthening of high entropy alloys by dilute solute additions: $CoCrFeNiAl_x$ and $CoCrFeNiMnAl_x$ alloys, Scr. Mater. **138**, 92 (2017).

[19] A. Tehranchi, B. Yin, and W. A. Curtin, Softening and hardening of yield stress by hydrogen-solute interactions, Philos. Mag. **97**, 400 (2017).

[20] G. Laplanche, J. Bonneville, C. Varvenne, W. Curtin, and E. P. George, Thermal activation parameters of plastic flow reveal deformation mechanisms in the CrMnFeCoNi high-entropy alloy, Acta Mater. **143**, 257 (2018).

[21] G. Bracq, M. Laurent-Brocq, C. Varvenne, L. Perriúre, W. Curtin, J.-M. Joubert, and I. Guillot, Combining experiments

and modeling to explore the solid solution strengthening of high and medium entropy alloys, Acta Mater. **177**, 266 (2019).
[22] B. Yin and W. A. Curtin, Origin of high strength in the cocrfenipd high-entropy alloy, Mater. Res. Lett. **8**, 209 (2020).
[23] B. Yin, S. Yoshida, N. Tsuji, and W. A. Curtin, Yield strength and misfit volumes of NiCoCr and implications for short-range-order, Nat. Commun. **11**, 2507 (2020).
[24] P. Soven, Coherent-Potential Model of Substitutional Disordered Alloys, Phys. Rev. **156**, 809 (1967).
[25] B. Velický, S. Kirkpatrick, and H. Ehrenreich, Single-site approximations in the electronic theory of simple binary alloys, Phys. Rev. **175**, 747 (1968).
[26] J. P. Perdew, S. Kurth, A. Zupan, and P. Blaha, Accurate Density Functional with Correct Formal Properties: A Step Beyond the Generalized Gradient Approximation, Phys. Rev. Lett. **82**, 2544 (1999).
[27] J. Tao, J. P. Perdew, V. N. Staroverov, and G. E. Scuseria, Climbing the Density Functional Ladder: Nonempirical Meta–Generalized Gradient Approximation Designed for Molecules and Solids, Phys. Rev. Lett. **91**, 146401 (2003).
[28] Y. Zhao and D. G. Truhlar, A new local density functional for main-group thermochemistry, transition metal bonding, thermochemical kinetics, and noncovalent interactions, J. Chem. Phys. **125**, 194101 (2006).
[29] J. P. Perdew, A. Ruzsinszky, G. I. Csonka, O. A. Vydrov, G. E. Scuseria, L. A. Constantin, X. Zhou, and K. Burke, Restoring the Density-Gradient Expansion for Exchange in Solids and Surfaces, Phys. Rev. Lett. **100**, 136406 (2008).
[30] J. Sun, A. Ruzsinszky, and J. P. Perdew, Strongly Constrained and Appropriately Normed Semilocal Density Functional, Phys. Rev. Lett. **115**, 036402 (2015).
[31] A. D. Becke, Exploring the limits of gradient corrections in density functional theory, J. Comput. Chem. **20**, 63 (1999).
[32] Z. Wu and R. E. Cohen, More accurate generalized gradient approximation for solids, Phys. Rev. B **73**, 235116 (2006).
[33] V. Razumovskiy, C. Hahn, M. Lukas, and L. Romaner, *Ab Initio* study of elastic and mechanical properties in FeCrMn alloys, Materials (Basel) **12**, 1129 (2019).
[34] A. van de Walle and G. Ceder, Correcting overbinding in local-density-approximation calculations, Phys. Rev. B **59**, 14992 (1999).
[35] J. P. Perdew, K. Burke, and M. Ernzerhof, Generalized Gradient Approximation Made Simple, Phys. Rev. Lett. **77**, 3865 (1996).
[36] J. P. Perdew and Y. Wang, Accurate and simple analytic representation of the electron-gas correlation energy, Phys. Rev. B **45**, 13244 (1992).
[37] L. Vitos, Total-energy method based on the exact muffin-tin orbitals theory, Phys. Rev. B **64**, 014107 (2001).
[38] A. V. Ruban and M. Dehghani, Atomic configuration and properties of austenitic steels at finite temperature: Effect of longitudinal spin fluctuations, Phys. Rev. B **94**, 104111 (2016).
[39] I. A. Abrikosov, S. I. Simak, B. Johansson, A. V. Ruban, and H. L. Skriver, Locally self-consistent green's function approach to the electronic structure problem, Phys. Rev. B **56**, 9319 (1997).
[40] O. E. Peil, A. V. Ruban, and B. Johansson, Self-consistent supercell approach to alloys with local environment effects, Phys. Rev. B **85**, 165140 (2012).
[41] L. Vitos, J. Kollár, and H. L. Skriver, Full charge-density scheme with a kinetic-energy correction: Application to ground-state properties of the 4d metals, Phys. Rev. B **55**, 13521 (1997).
[42] B. Gyorffy, A. Pindor, J. Staunton, G. Stocks, and H. Winter, A first-principles theory of ferromagnetic phase transitions in metals, J. Phys. F: Met. Phys. **15**, 1337 (1985).
[43] A. V. Ruban, A. B. Belonoshko, and N. V. Skorodumova, Impact of magnetism on Fe under Earth's core conditions, Phys. Rev. B **87**, 014405 (2013).
[44] V. I. Razumovskiy, A. Reyes-Huamantinco, P. Puschnig, and A. V. Ruban, Effect of thermal lattice expansion on the stacking fault energies of fcc Fe and $Fe_{75}Mn_{25}$ alloy, Phys. Rev. B **93**, 054111 (2016).
[45] E. Kabliman, P. Blaha, K. Schwarz, O. E. Peil, A. V. Ruban, and B. Johansson, Configurational thermodynamics of the Fe-Cr σ phase, Phys. Rev. B **84**, 184206 (2011).
[46] Z. Dong, S. Schönecker, D. Chen, W. Li, M. Long, and L. Vitos, Elastic properties of paramagnetic austenitic steel at finite temperature: Longitudinal spin fluctuations in multicomponent alloys, Phys. Rev. B **96**, 174415 (2017).
[47] V. L. Moruzzi, J. F. Janak, and K. Schwarz, Calculated thermal properties of metals, Phys. Rev. B **37**, 790 (1988).
[48] P. A. Korzhavyi, A. V. Ruban, S. I. Simak, and Y. K. Vekilov, Electronic structure, thermal, and elastic properties of Al-Li random alloys, Phys. Rev. B **49**, 14229 (1994).
[49] J.-W. Hwang, Thermal expansion of nickel and iron, and the influence of nitrogen on the lattice parameter of iron at the Curie temperature, Ph.D. thesis, University of Missouri–Rolla, 1972.
[50] H. M. Ledbetter and R. P. Reed, Elastic properties of metals and alloys, I. Iron, Nickel, and Iron-Nickel alloys, J. Phys. Chem. Ref. Data **2**, 531 (1973).
[51] M. Gao, J. Yeh, P. Liaw, and Y. Zhang, *High-Entropy Alloys: Fundamentals and Applications*, Vol. 1 (Springer, Berlin, 2016).
[52] A. Haglund, M. Koehler, D. Catoor, E. George, and V. Keppens, Polycrystalline elastic moduli of a high-entropy alloy at cryogenic temperatures, Intermetallics **58**, 62 (2015).
[53] G. R. Speich, A. J. Schwoeble, and W. C. Leslie, Elastic constants of binary iron-base alloys, Metall. Trans. **3**, 2031 (1972).
[54] H. Zhang, G. Wang, M. P. J. Punkkinen, S. Hertzman, B. Johansson, and L. Vitos, Elastic anomalies in Fe–Cr alloys, J. Phys.: Condens. Matter **25**, 195501 (2013).
[55] A. Landa, J. E. Klepeis, R. E. Rudd, K. J. Caspersen, and D. A. Young, Analytic binary alloy volume–concentration relations and the deviation from Zen's law, Appl. Sci. **11**, 6231 (2021).
[56] V. Sliwko, P. Mohn, and K. Schwarz, The electronic and magnetic structures of alpha-and beta-manganese, J. Phys.: Condens. Matter **6**, 6557 (1994).
[57] H. Park, A. J. Millis, and C. A. Marianetti, Density functional versus spin-density functional and the choice of correlated subspace in multivariable effective action theories of electronic structure, Phys. Rev. B **92**, 035146 (2015).
[58] E.-W. Huang, H.-S. Chou, K. N. Tu, W.-S. Hung, T.-N. Lam, C.-W. Tsai, C.-Y. Chiang, B.-H. Lin, A.-C. Yeh, S.-H. Chang, Y.-J. Chang, J.-J. Yang, X.-Y. Li, C.-S. Ku, K. An, Y.-W. Chang, and Y.-L. Jao, Element effects on high-entropy alloy vacancy and

heterogeneous lattice distortion subjected to quasi-equilibrium heating, Sci. Rep. **9**, 14788 (2019).

[59] M. S. Lucas, G. B. Wilks, L. Mauger, J. A. Muñoz, O. N. Senkov, E. Michel, J. Horwath, S. L. Semiatin, M. B. Stone, D. L. Abernathy, and E. Karapetrova, Absence of long-range chemical ordering in equimolar FeCoCrNi, Appl. Phys. Lett. **100**, 251907 (2012).

[60] J. Brechtl and P. K. Liaw, High-entropy materials: Theory, experiments, and applications, Springer **1**, 446 (2022).

[61] C. Varvenne, A. Luque, W. G. Nöhring, and W. A. Curtin, Average-atom interatomic potential for random alloys, Phys. Rev. B **93**, 104201 (2016).

[62] V. I. Razumovskiy, A. V. Ruban, and P. A. Korzhavyi, First-principles study of elastic properties of Cr- and Fe-rich Fe-Cr alloys, Phys. Rev. B **84**, 024106 (2011).

[63] V. I. Razumovskiy, A. V. Ruban, and P. A. Korzhavyi, Effect of Temperature on the Elastic Anisotropy of Pure Fe and $Fe_{0.9}Cr_{0.1}$ Random Alloy, Phys. Rev. Lett. **107**, 205504 (2011).

[64] H. Song, F. Tian, Q.-M. Hu, L. Vitos, Y. Wang, J. Shen, and N. Chen, Local lattice distortion in high-entropy alloys, Phys. Rev. Mater. **1**, 023404 (2017).

[65] L.-Y. Tian, Q.-M. Hu, R. Yang, J. Zhao, B. Johansson, and L. Vitos, Elastic constants of random solid solutions by SQS and CPA approaches: the case of fcc Ti-Al, J. Phys.: Condens. Matter **27**, 315702 (2015).

[66] K. Jin, B. C. Sales, G. M. Stocks, G. D. Samolyuk, M. Daene, W. J. Weber, Y. Zhang, and H. Bei, Tailoring the physical properties of Ni-based single-phase equiatomic alloys by modifying the chemical complexity, Sci. Rep. **6**, 20159 (2016).

[67] Z. Wu, Y. Gao, and H. Bei, Thermal activation mechanisms and labusch-type strengthening analysis for a family of high-entropy and equiatomic solid-solution alloys, Acta Mater. **120**, 108 (2016).

[68] F. Otto, A. Dlouhy, C. Somsen, H. Bei, G. Eggeler, and E. George, The influences of temperature and microstructure on the tensile properties of a cocrfemnni high-entropy alloy, Acta Mater. **61**, 5743 (2013).

[69] B. Uzer, S. Picak, J. Liu, T. Jozaghi, D. Canadinc, I. Karaman, Y. Chumlyakov, and I. Kireeva, On the mechanical response and microstructure evolution of NiCoCr single crystalline medium entropy alloys, Mater. Res. Lett. **6**, 442 (2018).

[70] Z. Wu, Y. Gao, and H. Bei, Single crystal plastic behavior of a single-phase, face-center-cubic-structured, equiatomic fenicrco alloy, Scr. Mater. **109**, 108 (2015).

[71] N. L. Okamoto, S. Fujimoto, Y. Kambara, M. Kawamura, Z. M. T. Chen, H. Matsunoshita, K. Tanaka, H. Inui, and E. P. George, Size effect, critical resolved shear stress, stacking fault energy, and solid solution strengthening in the CrMnFeCoNi high-entropy alloy, Sci. Rep. **6**, 35863 (2016).

[72] W. Abuzaid and H. Sehitoglu, Critical resolved shear stress for slip and twin nucleation in single crystalline FeNiCoCrMn high entropy alloy, Mater. Charact. **129**, 288 (2017).

[73] M. Kawamura, M. Asakura, N. L. Okamoto, K. Kishida, H. Inui, and E. P. George, Plastic deformation of single crystals of the equiatomic Cr-Mn-Fe-Co-Ni high-entropy alloy in tension and compression from 10k to 1273k, Acta Mater. **203**, 116454 (2021).

[74] K. Jin, Y. Gao, and H. Bei, Intrinsic properties and strengthening mechanism of monocrystalline Ni-containing ternary concentrated solid solutions, Mater. Sci. Eng.: A **695**, 74 (2017).

[75] Z. Wu, H. Bei, G. Pharr, and E. George, Temperature dependence of the mechanical properties of equiatomic solid solution alloys with face-centered cubic crystal structures, Acta Mater. **81**, 428 (2014).

[76] C. Wagner, A. Ferrari, J. Schreuer, J.-P. Couzinie, Y. Ikeda, F. Körmann, G. Eggeler, E. P. George, and G. Laplanche, Effects of Cr/Ni ratio on physical properties of Cr-Mn-Fe-Co-Ni high-entropy alloys, Acta Mater. **227**, 117693 (2022).

[77] G. Laplanche, M. Schneider, F. Scholz, J. Frenzel, G. Eggeler, and J. Schreuer, Processing of a single-crystalline crconi medium-entropy alloy and evolution of its thermal expansion and elastic stiffness coefficients with temperature, Scr. Mater. **177**, 44 (2020).

[78] X. Liu, Z. Pei, and M. Eisenbach, Dislocation core structures and Peierls stresses of the high-entropy alloy NiCoFeCrMn and its subsystems, Mater. Design **180**, 107955 (2019).

[79] V. Chaudhary, V. Soni, B. Gwalani, R. Ramanujan, and R. Banerjee, Influence of non-magnetic Cu on enhancing the low temperature magnetic properties and curie temperature of FeCoNiCrCu(x) high entropy alloys, Scr. Mater. **182**, 99 (2020).

[80] D. Gambino, M. Arale Brännvall, A. Ehn, Y. Hedström, and B. Alling, Longitudinal spin fluctuations in BCC and liquid Fe at high temperature and pressure calculated with a supercell approach, Phys. Rev. B **102**, 014402 (2020).

[81] B. Huck, F. Saurenbach, and J. Hesse, Investigation of spin structure in fcc Fe-Ni-Mn, Hyperfine Interact. **28**, 479 (1986).

[82] A. V. Ruban, P. A. Korzhavyi, and B. Johansson, First-principles theory of magnetically driven anomalous ordering in bcc Fe-Cr alloys, Phys. Rev. B **77**, 094436 (2008).

[83] Z. Li and D. Raabe, Strong and ductile non-equiatomic high-entropy alloys: Design, processing, microstructure, and mechanical properties, JOM **69**, 2099 (2017).

[84] M. Laurent-Brocq, L. Perrière, R. Pirś, and Y. Champion, From high entropy alloys to diluted multi-component alloys: Range of existence of a solid-solution, Mater. Design **103**, 84 (2016).

[85] O. Schneeweiss, M. Friák, M. Dudová, D. Holec, M. Šob, D. Kriegner, V. Holý, P. Beran, E. P. George, J. Neugebauer, and A. Dlouhý, Magnetic properties of the CrMnFeCoNi high-entropy alloy, Phys. Rev. B **96**, 014437 (2017).

[86] G. Laplanche, S. Berglund, C. Reinhart, A. Kostka, F. Fox, and E. George, Phase stability and kinetics of σ-phase precipitation in CrMnFeCoNi high-entropy alloys, Acta Mater. **161**, 338 (2018).

[87] E. Pickering, R. Muñoz-Moreno, H. Stone, and N. Jones, Precipitation in the equiatomic high-entropy alloy CrMnFeCoNi, Scr. Mater. **113**, 106 (2016).

[88] F. Otto, A. Dlouhy, K. Pradeep, M. Kubenová, D. Raabe, G. Eggeler, and E. George, Decomposition of the single-phase high-entropy alloy CrMnFeCoNi after prolonged anneals at intermediate temperatures, Acta Mater. **112**, 40 (2016).

[89] B. Schönfeld, C. R. Sax, J. Zemp, M. Engelke, P. Boesecke, T. Kresse, T. Boll, T. Al-Kassab, O. E. Peil, and A. V. Ruban, Local order in Cr-Fe-Co-Ni: Experiment and electronic structure calculations, Phys. Rev. B **99**, 014206 (2019).

[90] F. D. C. Garcia Filho, R. O. Ritchie, M. A. Meyers, and S. N. Monteiro, Cantor-derived medium-entropy

alloys: bridging the gap between traditional metallic and high-entropy alloys, J. Mater. Res. Technol. **17**, 1868 (2022).
[91] E. Zen, Validity of Vegard's law, Am. Mineral. **41**, 523 (1956).
[92] A. V. Ruban, H. L. Skriver, and J. K. Nørskov, Crystal-Structure Contribution to the Solid Solubility in Transition Metal Alloys, Phys. Rev. Lett. **80**, 1240 (1998).
[93] D. G. Pettifor, *Bonding and Structure of Molecules and Solids* (Oxford University Press, Oxford, 1995).
[94] D. Pettifor, in *Solid State Physics, Vol. 40, edited by H. Ehrenreich and D. Turnbull* (Elsevier, Amsterdam, 1987).
[95] H. A. Moreen, R. Taggart, and D. H. Polonis, A model for the prediction of lattice parameters of solid solutions, Metall. Trans. **2**, 265 (1971).